horticulturae

MDPI

Article

Integrated Physiological, Transcriptomic, and MALDI-MSI Analyses Reveal the Response Mechanisms of *Corydalis saxicola* Bunting Under Long-Term High-Calcium Conditions

Chang Liu [1], Hongzhuan Shi [1], Yu Du [1], Qingjun Zou [1], Tao Wang [1], Kaijun Zhao [2] and Qiaosheng Guo [1,*]

[1] Institute of Chinese Medicinal Materials, Nanjing Agricultural University, Nanjing 210014, China
[2] Nanjing Zhongshan Pharmaceutical Co., Ltd., Nanjing 210046, China
* Correspondence: gqs@njau.edu.cn

Highlights

What are the main findings?

- In *Corydalis saxicola*, long-term $CaCl_2$ treatment altered root Ca^{2+} fluxes, increased tissue calcium concentrations, and shifted subcellular calcium partitioning.
- $CaCl_2$ treatment increased root benzylisoquinoline alkaloid concentrations in *C. saxicola* and was associated with changes in putatively annotated metabolite ion distributions.

What are the implications of the main findings?

- Tissue calcium homeostasis, antioxidant responses, and specialized metabolism are associated components of the response to prolonged $CaCl_2$ exposure.
- Candidate calcium-signaling and alkaloid-biosynthesis genes provide targets for functional validation.

Abstract

Corydalis saxicola Bunting is a medicinal herb native to karst habitats in southwestern China, where plants encounter calcium-rich substrates. Its coordinated physiological and specialized-metabolic responses to prolonged high calcium remain poorly understood. Plants were grown for six months under Control conditions, 100 mM $CaCl_2$ (Calcium), or 100 mM $CaCl_2$ plus 100 mM ethylene glycol-bis(β-aminoethyl ether)-N,N,N′,N′-tetraacetic acid (EGTA). Root and leaf physiology, calcium concentrations, alkaloids, and transcriptomes were assessed alongside root, stem, and leaf microscopy. Calcium treatment inhibited growth, altered tissue structure, increased proline and malondialdehyde, and induced tissue-specific antioxidant responses. Root-surface ion-flux measurements showed a reversal from weak net Ca^{2+} influx to strong efflux. Inductively coupled plasma optical emission spectrometry showed increased calcium concentrations in both tissues, with a greater fold increase in roots, and a shift in subcellular calcium proportions toward soluble fractions. Total alkaloid assays and high-performance liquid chromatography showed increased total alkaloids and three target compounds, with a larger total-alkaloid concentration response in roots. Matrix-assisted laser desorption/ionization mass spectrometry imaging (MALDI-MSI) revealed predominantly peripheral root signals for putatively annotated benzylisoquinoline alkaloid precursors and intermediates, with treatment-associated spatial changes. Transcriptome analysis and reverse transcription quantitative PCR identified tissue-specific expression changes in calcium transport and signaling candidates and increased expression of selected alkaloid-biosynthetic candidates in roots. These findings connect tissue calcium accumulation, physiological responses, and spatially organized specialized metabolism during prolonged $CaCl_2$ exposure, providing candidate processes and genes for understanding the responses of *C. saxicola* to calcium-rich environments.

Check for updates

Academic Editor: David P. Horvath

Received: 9 October 2026
Revised: 10 November 2026
Accepted: 17 November 2026
Published: 18 November 2026

Copyright: © 2026 by the authors. Licensee MDPI, Basel, Switzerland. This article is an open access article distributed under the terms and conditions of the Creative Commons Attribution (CC BY) license.

Keywords: *Corydalis saxicola* Bunting; calcium homeostasis; benzylisoquinoline alkaloids; MALDI-MSI; RNA-Seq

1. Introduction

Calcium is an essential mineral nutrient for plant growth and development and an important second messenger in plant cells. It contributes to cell-wall construction and plasma-membrane stability and influences cell division, elongation, and tissue development. Environmental stimuli also induce changes in the amplitude, frequency, duration, and spatial distribution of free Ca^{2+} concentrations in the cytosol and organelles, creating characteristic calcium signatures. These signals are sensed and decoded by calmodulins, calmodulin-like proteins, calcium-dependent protein kinases, and calcineurin B-like proteins, thereby regulating plant growth, metabolism, and stress responses [1,2].

Plant cells must maintain cytosolic free Ca^{2+} at a low, relatively stable concentration while meeting structural and nutritional requirements. Extracellular Ca^{2+} enters cells through cyclic nucleotide-gated channels, glutamate receptor-like channels, and other Ca^{2+}-permeable channels. Ca^{2+}-ATPases and Ca^{2+}/H^{+} antiporters transport cytosolic Ca^{2+} into intracellular stores, including the vacuole and endoplasmic reticulum, or export it from the cell. Recent work showed that the Arabidopsis calcineurin B-like protein–CBL-interacting protein kinase (CBL-CIPK) signaling module activates tonoplast cation/H^{+} exchanger (CAX) proteins through phosphorylation, promoting the sequestration of excess cytosolic Ca^{2+} in vacuoles and coordinating calcium homeostasis, growth, and immunity under high external calcium [3].

Moderate calcium availability supports the functions of cell walls, membranes, and organelles, whereas excess external Ca^{2+} can be toxic [1], causing cytosolic calcium overload, mineral imbalance, membrane disruption, and growth inhibition [2]. Environmental stress is also commonly accompanied by the accumulation of reactive oxygen species (ROS). When ROS production exceeds the plant's scavenging capacity, it can cause membrane lipid peroxidation, protein oxidation, and organelle damage. Plants limit oxidative injury through antioxidant enzymes, including superoxide dismutase (SOD), peroxidase (POD), and catalase (CAT), and through osmotic and redox regulators such as proline. Malondialdehyde (MDA) is a product of membrane lipid peroxidation. Measuring MDA alongside antioxidant activity, proline accumulation, and structural changes helps assess membrane oxidative injury during prolonged $CaCl_2$ exposure [4–6].

Corydalis saxicola Bunting is a perennial herb of the Papaveraceae that grows mainly on limestone cliffs, in rock crevices and caves, and near sinkholes in the karst regions of southwestern China [7]. It is valuable both as a medicinal plant and as a model for ecological adaptation to karst environments. Karst habitats generally have shallow soil, limited water-holding capacity, alkaline substrates, and high calcium availability. Long-term exposure to these conditions may have selected specialized mechanisms of calcium uptake, transport, tissue accumulation, and intracellular homeostasis in *C. saxicola* [7].

In contrast to model plants and crops such as Arabidopsis, rice, and tomato, the physiological and molecular responses of *C. saxicola* to high calcium have not been studied systematically. The species is rich in isoquinoline alkaloids, and its chemical composition and bioactivity vary with genotype, tissue, and growing environment [8]. A 2024 study of the *C. saxicola* mitochondrial genome provided initial evidence linking calcium treatment to genetic and metabolic responses [9]. Exogenous $CaCl_2$ altered the expression of several mitochondrial core protein-coding genes and was associated with changes in root dehydrocavidine content, suggesting that calcium availability may affect both energy metabolism

and medicinal specialized metabolism. That study, however, focused on the mitochondrial genome and selected mitochondrial transcripts and did not resolve rhizosphere ion dynamics, tissue calcium concentrations, cellular ultrastructure, or transcriptome-wide responses.

Corydalis saxicola is also used in ethnomedicine in southwestern China. Its major active constituents are isoquinoline alkaloids, including protoberberine-type compounds; dehydrocavidine, berberine, and palmatine are representative constituents of particular interest [10–12]. Wild and cultivated plants can differ in chemical composition and content, indicating that both genetic background and environmental conditions affect the accumulation of medicinal compounds [8]. Understanding how calcium availability influences alkaloid accumulation is therefore relevant to both ecological adaptation and medicinal plant quality.

Accordingly, this study compared control, high-calcium, and calcium-chelation treatments and integrated physiological and biochemical assays, microscopy, ion-flux measurements, elemental analysis, chemical profiling, mass spectrometry imaging, and transcriptomics. The objectives were to (1) characterize physiological, biochemical, and structural changes under high calcium; (2) determine root-surface Ca^{2+} fluxes, root and leaf calcium concentrations and subcellular calcium partitioning, and the abundance and spatial distribution of isoquinoline alkaloids; and (3) identify candidate genes and assess their expression in relation to calcium homeostasis and isoquinoline alkaloid metabolism. Together, these analyses were used to develop a physiological–metabolic–molecular framework for the response of *C. saxicola* to prolonged $CaCl_2$ exposure.

2. Materials and Methods

2.1. Plant Material, Growth Conditions, and Calcium Treatments

Seeds of *C. saxicola* were collected in 2020 in Donglan County, Guangxi Zhuang Autonomous Region, China (107°14′39″ E, 24°26′15″ N), and identified by Professor Qiaosheng Guo of Nanjing Agricultural University. After collection, the seeds were stored in a cool cabinet at 4 °C and 40% relative humidity. Before the experiment, seeds were sown in seedling trays filled with substrate purchased from Jiangsu Xingnong Substrate Technology Co., Ltd., Lianyungang, China. (batch 37119Q0172R2S), which was kept moist each day. Healthy, disease-free seedlings of uniform vigor with three to five true leaves were transplanted individually into pots (20 cm diameter, 18 cm height). Plants were grown in a controlled growth room at the Institute of Chinese Medicinal Materials, Nanjing Agricultural University, Nanjing, China, at 25 °C, 50% relative humidity, and a 16 h light/8 h dark photoperiod. Each pot received 500 mL deionized water every 5 d and a general-purpose horticultural nutrient solution every 30 d. Three treatments were established: (1) Control, deionized water; (2) Calcium, 100 mM $CaCl_2$ in the watering solution; and (3) EGTA, 100 mM $CaCl_2$ plus 100 mM EGTA in the watering solution.

EGTA (ethylene glycol-bis(β-aminoethyl ether)-N,N,N′,N′-tetraacetic acid; $C_{14}H_{24}N_2O_{10}$) was used as a chelator with preferential binding to Ca^{2+} over Mg^{2+} [13]. EGTA was dissolved in deionized water at room temperature, and the final EGTA irrigation solution containing 100 mM $CaCl_2$ and 100 mM EGTA was adjusted to pH 6.0 with 1 M HCl and 5 M KOH. Free Ca^{2+} in the undiluted EGTA irrigation solution was measured directly using a calcium ion-selective electrode connected to a PXSJ-216F ion meter (LEICI, Shanghai, China), calibrated with a 100 mg L^{-1} Ca^{2+} standard solution. The three measurements were 1.5677, 1.5334, and 1.4935 mM, giving a mean ± SD of 1.5315 ± 0.0371 mM ($n = 3$). Free Ca^{2+} concentrations in the three irrigation solutions are compared in Figure S1A.

Two independent six-month cultivation and treatment runs were initiated in December 2022 and February 2023. Each run included 20 pots per treatment, with one plant per pot. Plants were maintained on different racks in the same controlled growth room under the

same light, humidity, and watering conditions. Plants used for each assay were randomly selected from the corresponding treatment group. Each biological replicate represented a different plant; root and leaf samples were paired from the same plant, and the different assays used plants from the same cultivation cohort. All non-RNA-seq assays were performed in both runs, with consistent principal trends. Quantitative summaries and representative images presented here are from the second run; results were not pooled across runs. RNA-seq samples were collected from the second run in August 2023. Each assay used three independent biological replicates per treatment and tissue, except the non-invasive micro-test technology (NMT) assay, which used six independent plants per treatment.

For physiological and biochemical assays, subcellular calcium fractionation, RNA-seq, and reverse transcription quantitative PCR (RT-qPCR), whole root systems were cleaned of soil and debris, and normally growing leaves were collected, excluding very small young leaves and visibly senescent or wilted leaves. Fresh samples for physiological assays were ground and homogenized on ice. For tissue calcium, total alkaloid, and high-performance liquid chromatography (HPLC) analyses, entire cleaned root systems and all leaves collected from the stems were dried at 50 °C and ground separately into powders; stems were not included in the leaf samples. Root, stem, and leaf tissues were collected for microscopy and stored in fixative. Samples for RNA analyses were frozen immediately in liquid nitrogen and stored at −80 °C. Main roots were sampled for frozen transverse sections for MALDI-MSI, as described in Section 2.10.

2.2. Tissue Morphology and Ultrastructure

Transmission electron microscopy (TEM). Fixed samples were rinsed three times for 15 min each in 0.1 M phosphate buffer (pH 7.4). After fixation and dehydration, samples were embedded in resin, and 60 nm ultrathin sections were prepared with a Leica UC7 ultramicrotome. Sections were stained in the dark with 2% uranyl acetate in saturated ethanol, dried, examined with a HITACHI HT7800 transmission electron microscope, and imaged. Root and leaf tissues from three independent plants per treatment were examined; representative images are presented.

Scanning electron microscopy (SEM). Fixed samples were rinsed three times for 15 min each in 0.1 M phosphate buffer (pH 7.4). After fixation and dehydration, samples were dried in a Quorum K850 critical-point dryer (Quorum Technologies Ltd., Laughton, UK), mounted on conductive double-sided carbon tape, and sputter-coated with gold for approximately 30 s using a HITACHI MC1000 ion(Hitachi High-Tech Corporation, Tokyo, Japan) sputter coater. Samples were examined and imaged with a HITACHI SU8100(Hitachi High-Tech Corporation, Tokyo, Japan) scanning electron microscope. Root, stem, and leaf tissues from three independent plants per treatment were examined; representative images are presented.

2.3. Physiological and Biochemical Measurements

All physiological and biochemical measurements were performed on fresh whole-root and leaf samples selected as described in Section 2.1. Samples were processed on ice, three independent plants per treatment and tissue were analyzed for each variable, and results were normalized to fresh weight. Proline was measured by the acid-ninhydrin method at 520 nm and quantified from a standard curve. MDA was measured with a malondialdehyde assay kit (Solarbio, Beijing, China) according to the manufacturer's instructions, with absorbance recorded at 532 and 600 nm. CAT activity was measured at 240 nm using a catalase assay kit (BC0205, Solarbio, Beijing, China). POD activity was measured at 470 nm using a peroxidase assay kit (BC0095, Solarbio, Beijing, China), and SOD activity was measured at 560 nm using a superoxide dismutase assay kit (BC0170, Solarbio, Beijing,

China). Absorbance was recorded with a microplate reader (BioTek Instruments, Winooski, VT, USA) and a UV-visible spectrophotometer (model 752, Jinghua, Shanghai, China).

2.4. Calcium Content and Root-Surface Ca^{2+} Flux

For total calcium determination, 0.5 g of dried root or leaf powder was transferred to a digestion tube, mixed with 10 mL nitric acid, and digested in a MARS 6 microwave digestion system (CEM, Matthews, NC, USA). The digest was diluted 250-fold, and calcium was quantified by inductively coupled plasma optical emission spectrometry (ICP-OES; iCAP 7400, Thermo Fisher Scientific, Waltham, MA, USA). Tissue calcium concentrations were expressed as g kg^{-1} dry weight. Three independent plants were analyzed per treatment, with roots and leaves sampled from each plant. At the final harvest after six months, pot-substrate samples were dried, acid-digested, and analyzed by ICP-OES to determine total calcium on a dry-weight basis (Figure S1B).

Plants were sampled after six months of treatment. Soil particles were removed from the roots with deionized water, and each root was fixed to the bottom of a Petri dish. The NMT test solutions were adjusted to pH 5.8 and contained: 0.2 mM 2-(N-morpholino)ethanesulfonic acid (MES) for Control; 100 mM $CaCl_2$ plus 0.2 mM MES for Calcium; and 100 mM $CaCl_2$, 100 mM EGTA, and 0.2 mM MES for EGTA. Root-surface net Ca^{2+} flux was measured for 5 min in the meristematic region of the root tip using an NMT Physiolyzer® system (YoungerUSA LLC, Amherst, MA, USA). Six independent plants (biological replicates) were measured per treatment, and flux data were read and exported directly with imFluxes v3.0.

2.5. Subcellular Distribution of Calcium

Subcellular calcium fractions were obtained according to Liu et al. [14]. Fresh root and leaf samples (0.5 g) were frozen, ground to particles smaller than 0.5 mm, and homogenized in 50 mmol L^{-1} Tris-HCl buffer (pH 7.5) containing 250 mmol L^{-1} sucrose, 1.0 mmol L^{-1} dithioerythritol (DTE; $C_4H_{10}O_2S_2$), and 5.0 mmol L^{-1} ascorbic acid. A refrigerated centrifuge (H2-16KR, Kecheng, Changsha, China) was maintained at 4 °C. Ten milliliters of homogenate was centrifuged at 4000× *g* for 15 min; the pellet was designated the cell-wall fraction. The supernatant was then centrifuged at 12,000× *g* for 40 min. The resulting supernatant and pellet were designated the soluble fraction and organelle-containing fraction, respectively. Calcium in each fraction was quantified by ICP-OES (iCAP 7400, Thermo Fisher Scientific). Root and leaf samples were obtained from three independent plants per treatment using the selection criteria in Section 2.1.

2.6. Total Alkaloid Content

Total alkaloids in dried whole-root and leaf powders from three independent plants per treatment were quantified with a total alkaloid assay kit (G0150F, Suzhou Grace Biotechnology Co., Ltd., Suzhou, China) according to the manufacturer's instructions, with absorbance measured at 415 nm.

2.7. Quantification of Three Isoquinoline Alkaloids

Dehydrocavidine, palmatine hydrochloride, and berberine hydrochloride were selected as target analytes with reference to Sun et al. [15]. Dried whole-root or leaf powder (0.2 g) was weighed into a stoppered conical flask, mixed with 50 mL of 1% hydrochloric acid in methanol, and sonicated at 500 W and 40 kHz for 15 min. After cooling, the lost mass was replaced with extraction solvent, and the solution was filtered through a 0.22 μm membrane. Reference standards of dehydrocavidine (batch 111667-200401, purity 100%), palmatine hydrochloride (batch 110732-201913, purity 85.7%), and berberine hydrochloride (batch

110713-202015, purity 85.9%) were obtained from the National Institutes for Food and Drug Control, Beijing, China. HPLC was performed on an LC-40D system (Shimadzu, Kyoto, Japan) equipped with a Waters XSelect CSH C18 column (250 mm × 4.6 mm, 5 µm). The mobile phase comprised acetonitrile (A) and 0.01 mol L^{-1} potassium dihydrogen phosphate (B), with the following gradient: 0–10 min, 20–25% A; 10–15 min, 25–30% A; 15–25 min, 30% A; 25–27 min, 30–20% A; and 27–30 min, 20% A. The flow rate was 1.0 mL min^{-1}, the detection wavelength was 347 nm, the column temperature was 30 °C, and the injection volume was 10 µL. Samples from three independent plants were analyzed per treatment and tissue.

2.8. Transcriptome Sequencing and Analysis

RNA-seq used three randomly selected plants per treatment from the second cultivation run. Whole-root and normally growing leaf samples were collected from each plant using consistent tissue-selection criteria (Section 2.1), producing 18 libraries (three treatments × two tissues × three independent biological replicates). Total RNA was isolated and purified with TRIzol reagent (15596018, Thermo Fisher Scientific) according to the manufacturer's protocol. RNA concentration and purity were assessed with a NanoDrop ND-1000 spectrophotometer (NanoDrop Technologies, Wilmington, DE, USA), and integrity was evaluated with an Agilent 2100 Bioanalyzer (Agilent Technologies, Santa Clara, CA, USA). Eukaryotic mRNA was enriched from qualified RNA with oligo(dT) magnetic beads and randomly fragmented. First-strand cDNA was synthesized from fragmented mRNA using random hexamer primers, followed by second-strand synthesis with buffer, dNTPs, RNase H, and DNA polymerase I. Double-stranded products were purified with AMPure XP beads (Beckman Coulter, Inc., Brea, CA, USA), and sticky ends were converted to blunt ends using T4 DNA polymerase and Klenow DNA polymerase. After 3′ adenylation and adapter ligation, fragments were selected with AMPure XP beads. The U-containing second strand was degraded with USER enzyme, and the final libraries were obtained by PCR amplification.

Qualified libraries were sequenced on an Illumina NovaSeq 6000 platform (Illumina, Inc., San Diego, CA, USA) with 150 bp paired-end reads (PE150). The transcriptome was assembled de novo with Trinity v2.15. All assembled unigenes were searched with DIAMOND v2.0.15 at an *E*-value threshold of 1×10^{-5} against the NCBI non-redundant protein, Gene Ontology, Swiss-Prot, KEGG, and eggNOG databases. Transcript abundance was quantified with Salmon v1.9.0 and expressed as transcripts per million. Differential expression analysis used unigene read counts in edgeR v3.40.2. Between-sample normalization used the trimmed mean of M-values (TMM) method with calcNormFactors(method = "TMM"). Negative-binomial generalized linear models were fitted with glmQLFit(), and quasi-likelihood F-tests were performed with glmQLFTest(). Roots and leaves were analyzed separately, using treatment as the explanatory factor. Pairwise contrasts and a joint three-treatment test were performed. Gene-level *p* values were adjusted with the Benjamini–Hochberg (BH) method. TPM values were used for expression summaries, not as input to the differential expression tests. For pairwise comparisons, differentially expressed genes (DEGs) were defined by a false discovery rate (FDR) < 0.05 and $|\log_2 \text{fold change}| \geq 1$. For the joint comparison among all three treatments, genes with FDR < 0.05 were retained without applying a fold-change threshold. Sample-level sequencing and quality-control statistics are provided in Table S1.

KEGG enrichment was performed separately for roots and leaves using unigenes identified by the joint three-treatment test (FDR < 0.05), with the 11,316 KEGG-annotated unigenes as the background. Pathway *p* values were adjusted by the BH method across all tested pathways within each tissue (138 root pathways and 139 leaf pathways); adjusted

$p < 0.05$ was considered significant. The 12 pathways with the smallest adjusted p values are displayed, including ranked pathways that did not meet this threshold. The joint test identifies expression differences among treatments without assigning a single upregulated or downregulated direction.

2.9. RT-qPCR

RNA was extracted from the same batch of fresh samples used for transcriptome sequencing, and cDNA was synthesized using the Evo M-MLV RT Mix Kit with gDNA Clean for qPCR Ver. 2 (Accurate Biotechnology, Changsha, China) according to the manufacturer's instructions. Each target gene was assayed in three independent biological replicates per treatment and tissue. RPL4 (ribosomal protein L4; TRINITY_DN1428_c0_g1), a housekeeping gene, was selected as the reference after integrated assessment of its transcriptomic annotation, expression, and pairwise differential expression statistics (Tables S2–S4); it was not classified as a DEG under the criteria used in this study. RT-qPCR was performed with the SYBR Green Premix Pro Taq HS qPCR Kit (Accurate Biotechnology, Changsha, China) on a StepOne Real-Time PCR System (Applied Biosystems, Foster City, CA, USA). The reaction mixture is provided in Table S5, and reference and target gene primer sequences are listed in Table S6.

2.10. Matrix-Assisted Laser Desorption/Ionization Mass Spectrometry Imaging

Main roots from three independent plants per treatment were transversely cryosectioned at 20 µm using a CM1950 cryostat (Leica Biosystems, Nussloch, Germany). Sections were transferred with a pre-cooled brush to pre-cooled indium tin oxide-coated slides and dried for 30 min. A 15 mg mL^{-1} solution of 2,5-dihydroxybenzoic acid (DHB) in acetonitrile/water (90:10, v/v) was applied uniformly with a TM-Sprayer matrix sprayer at 60 °C, 0.12 mL min^{-1}, and 8 psi for 25 cycles, with 5 s drying between cycles. Coated slides were mounted on the mass spectrometer target. Tissue regions were selected in DataImaging software (Bruker), the imaging resolution was set to 50 µm, and each region was divided into a two-dimensional array of measurement points. Spectra were acquired over m/z 50–1300 under constant laser energy using a timsTOF flex mass spectrometer equipped with a 10 kHz smartbeam 3D laser (Bruker Daltonics, Bremen, Germany). Relative ion signal intensities do not represent absolute metabolite concentrations. Raw data were imported into SCiLS Lab, normalized by the root mean square method, and converted into ion-intensity maps for each m/z [16]. Average MALDI-MSI mass spectra for the three treatments are provided in Figure S2. On-tissue MS/MS spectra were acquired for selected ions and compared with database reference spectra for L-tyrosine, dopamine, and scoulerine (Figure S3). These comparisons support putative annotations; the remaining three assignments were based on MS1 information. Compound names therefore denote putative assignments rather than identities confirmed with authentic standards. Ion assignments, formulas, adducts, matching modes, scores, and mass errors are summarized in Table S9. MS1 and MS2 in Table S9 denote the matching evidence used, not formal metabolite-identification confidence levels. Stereochemical configurations indicated in compound names were not independently established.

Database matching and scoring were performed using MetX 3.1 with an integrated database search. For MS1-only matching, the precursor search tolerance was 10 ppm and the software-reported MS1 score threshold was 0.6. For MS/MS-supported matching, the precursor search tolerance was 1500 ppm and the fragment-matching tolerance was 500 ppm. The composite score combined precursor and MS/MS components with weights of 0.3 and 0.7, respectively. The MS/MS component combined fragment, forward-search, and reverse-search scores with weights of 0.6, 0.2, and 0.2, respectively. The MS2-component and

composite-score thresholds were both 0.1. These weights describe the available software scoring framework; the component-score transformations are proprietary. The software-reported MS1 score was retained for MS1-only entries. Scores describe database-match similarity and are not probabilities of correct identification. Mass error was calculated as (observed m/z—theoretical m/z of the stated ion)/theoretical $m/z \times 10^6$; values are approximate because the reported observed m/z values were rounded to three decimal places.

2.11. Statistical Analysis

Microsoft Excel 2021 was used to record and organize raw data, and IBM SPSS Statistics 20 (IBM Corp., Armonk, NY, USA) was used for statistical analysis. Multiple groups were compared by one-way analysis of variance, followed by Tukey's post hoc test. Two independent groups were compared with Student's *t*-test. Differences were considered significant at $p < 0.05$. GraphPad Prism 9.5 was used to prepare graphs. Data are presented as the mean ± standard deviation (SD). For plant assays, n denotes independent plants, not repeated instrument readings. Unless otherwise specified, $n = 3$ per treatment and tissue; NMT used $n = 6$ per treatment. Treatment effects were assessed separately within each tissue. Repeated observations on one plant were not counted as additional biological replicates.

2.12. AI-Assisted Language Editing

DeepSeek (DeepSeek-V4.1-Flash, Hangzhou DeepSeek Artificial Intelligence Basic Technology Research Co., Ltd., Hangzhou, China) and ChatGPT (GPT-5.6-Sol, 2026 release; OpenAI, San Francisco, CA, USA) were used after the manuscript had been fully written by the authors solely for language polishing, i.e., checking and improving grammar, spelling, punctuation, and formatting.

3. Results

3.1. Plant Growth and Root Morphology

After six months of treatment, the Control, Calcium, and EGTA groups showed clear differences in whole-plant morphology (Figure 1A). Control plants grew well, with relatively expanded leaves and an intact canopy. Calcium-treated plants showed pronounced growth inhibition and signs of leaf water loss, wilting, or senescence. Plants in the EGTA treatment showed partial recovery relative to the Calcium treatment, with more leaves and improved canopy integrity. Root phenotypes also differed among treatments (Figure 1B). Control roots were dominated by slender lateral roots, whereas Calcium-treated roots were generally thicker and showed altered fine-root and lateral-root morphology. Fine-root number and branching were partially restored in the EGTA treatment. Thus, long-term $CaCl_2$ treatment produced visible inhibitory effects on both shoots and roots, and the addition of EGTA partly alleviated these effects.

3.2. Tissue Surfaces and Cellular Ultrastructure Under High Calcium

SEM showed that calcium treatment altered the morphology of root-tip surfaces, root transverse sections, stem epidermis, and leaf epidermis (Figure 2A–O). Root hairs were regularly distributed in the Control group, and the epidermis, cortex, and pericycle were clearly distinguishable in root transverse sections (Figure 2A,D). In the Calcium group, root-hair morphology and arrangement changed, tissue interfaces in root sections were disrupted, and local structural irregularities or enlarged intercellular spaces were evident (Figure 2B,E). Root-tip surfaces and transverse sections were partly restored in the EGTA group (Figure 2C,F). SEM images of stem and abaxial leaf epidermis showed altered stomatal complexes and epidermal cell surfaces after Calcium treatment; some cells were swollen, loosely arranged, or had more pronounced surface relief (Figure 2G–L). In leaf

transverse sections, the adaxial epidermis, palisade tissue, spongy tissue, and vascular bundles were clearly organized in the Control group. Calcium treatment altered mesophyll arrangement and intercellular spaces and reduced tissue integrity near vascular bundles, whereas the EGTA group retained a more regular organization than the Calcium group (Figure 2M–O).

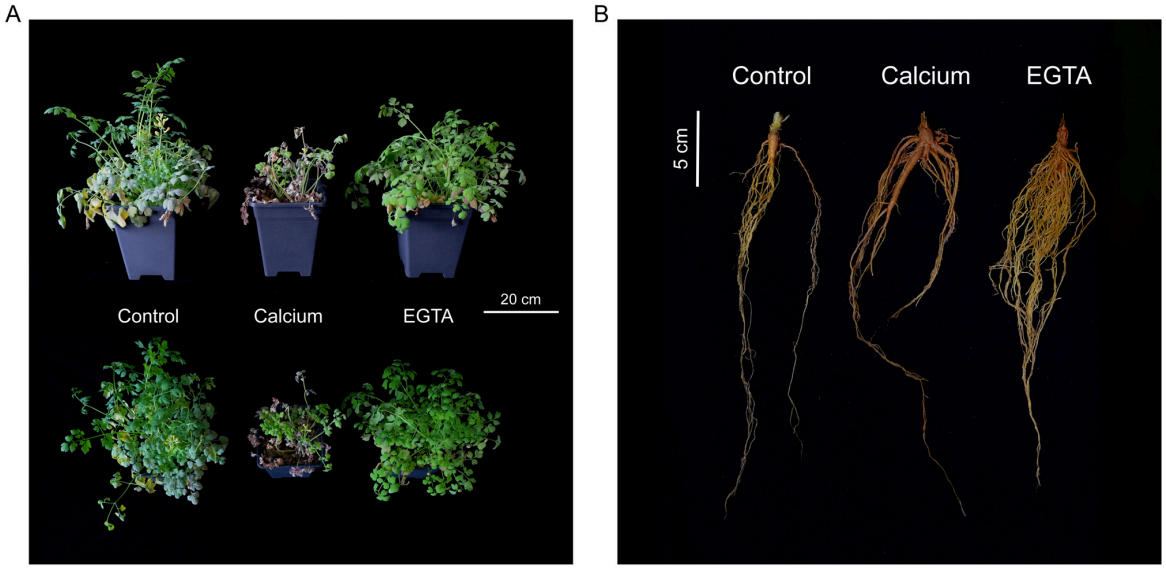


Figure 1. Morphology and root characteristics of *C. saxicola* under different calcium treatments. (**A**) Lateral and top views of potted plants (scale bar, 20 cm). (**B**) Root morphology after sampling (scale bar, 5 cm). Treatments were Control (deionized water), Calcium (100 mM $CaCl_2$), and EGTA (100 mM $CaCl_2$ plus 100 mM EGTA), applied for six months. Images are representative of three independent plants per treatment.

TEM further revealed calcium-induced changes in root and leaf cell ultrastructure (Figure 2P–U). Control root cells had intact walls, cytoplasm, nuclei, mitochondria, and vacuoles (Figure 2P). Calcium-treated root cells showed plasmolysis, condensed cytoplasm, peripheral aggregation of organelles, and more osmiophilic granules (Figure 2Q). Cytoplasmic and cell-wall structure was partly restored in EGTA-treated roots (Figure 2R). Mesophyll chloroplasts were well developed in the Control group, with clearly organized grana lamellae (Figure 2S). In the Calcium group, chloroplast degradation, disordered thylakoid organization, and greater starch-grain accumulation were observed (Figure 2T). Chloroplast structure was improved in the EGTA group relative to the Calcium group, although the images were assessed qualitatively (Figure 2U).

3.3. Antioxidant Defense, Lipid Peroxidation, and Proline Accumulation

Calcium treatment significantly altered antioxidant enzyme activities and stress-related biochemical variables in roots and leaves (Figure 3). SOD activity was higher in the Calcium group than in the Control group in both tissues. It decreased after EGTA treatment, remaining above or close to the Control level in roots and returning close to the Control level in leaves (Figure 3A). POD activity increased in Calcium-treated roots and leaves. With EGTA, root POD activity returned close to the Control level, whereas leaf activity declined further (Figure 3B). Root CAT responded differently from SOD and POD: activity was markedly lower in the Calcium group than in the Control group and significantly higher in the EGTA group. Leaf CAT activity decreased slightly with Calcium and was highest with EGTA (Figure 3C). Calcium significantly increased MDA content in roots and leaves, indicating greater membrane lipid peroxidation under long-term high calcium (Figure 3D). MDA

decreased with EGTA; root values remained above Control, whereas leaf values returned close to Control. Proline content increased significantly in Calcium-treated roots and leaves and returned close to Control with EGTA (Figure 3E). Overall, high calcium induced SOD and POD activity and proline accumulation, but the simultaneous rise in MDA indicated that these defenses did not fully prevent oxidative stress. The contrasting CAT responses and degree of MDA recovery demonstrate tissue-specific responses.

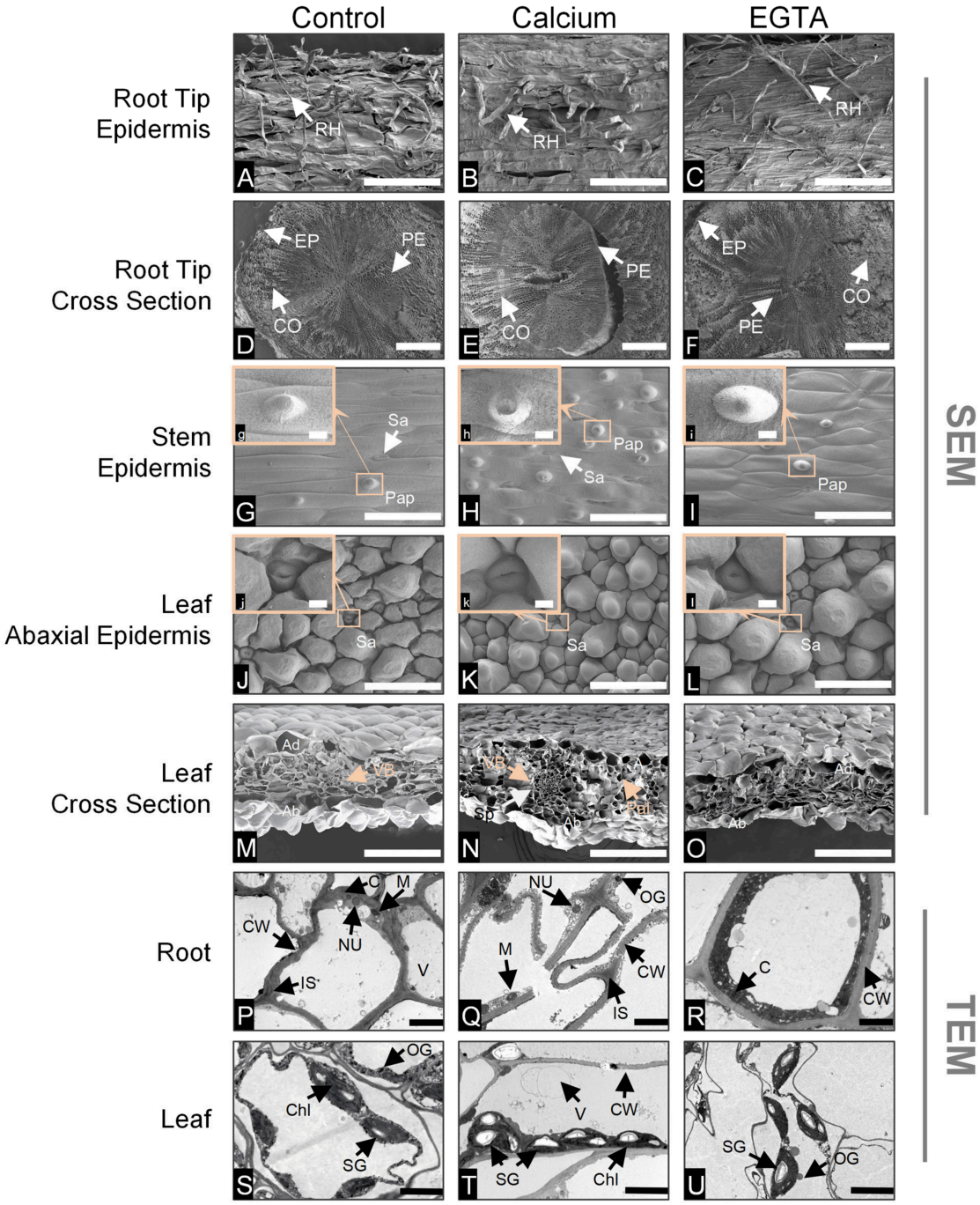


Figure 2. Scanning electron microscopy (SEM; (**A**–**O**)) and transmission electron microscopy (TEM; (**P**–**U**)) of *C. saxicola* roots, stems, and leaves under different calcium treatments. (**A**–**C**) Root-tip epidermal surface; (**D**–**F**) root-tip transverse section; (**G**–**I**) stem epidermal surface; (g–i) enlarged detail of Pap; (**J**–**L**) abaxial leaf epidermis and enlarged detail; (j–l) enlarged detail of Sa (**M**–**O**) leaf transverse section; (**P**–**R**) root-cell ultrastructure; (**S**–**U**) mesophyll-cell ultrastructure. Each row shows

Control, Calcium, and EGTA from (**left**) to (**right**). RH, root hair; EP, epidermis; PE, pericycle; CO, cortex; Sa, stomatal apparatus; Pap, papilla; Ad, adaxial epidermis; Ab, abaxial epidermis; VB, vascular bundle; SP, spongy tissue; Pal, palisade tissue; CW, cell wall; C, cytoplasm; M, mitochondrion; NU, nucleus; V, vacuole; IS, intercellular space; OG, osmiophilic granule; Chl, chloroplast; SG, starch grain. Scale bars: (**A**–**C**), 200 μm; (**D**–**F**), 1 mm; (**G**–**I**), 200 μm (g–i, 20 μm); (**J**–**L**), 100 μm (j–l, 10 μm); (**M**–**O**), 100 μm; (**P**–**R**), 2 μm; (**S**–**U**), 5 μm. Control tissues retained more regular organization; Calcium-treated tissues showed surface irregularities and ultrastructural disruption, with partial improvement in the EGTA group. Treatments were Control (deionized water), Calcium (100 mM $CaCl_2$), and EGTA (100 mM $CaCl_2$ plus 100 mM EGTA), applied for six months. Representative images from three independent plants per treatment are shown.

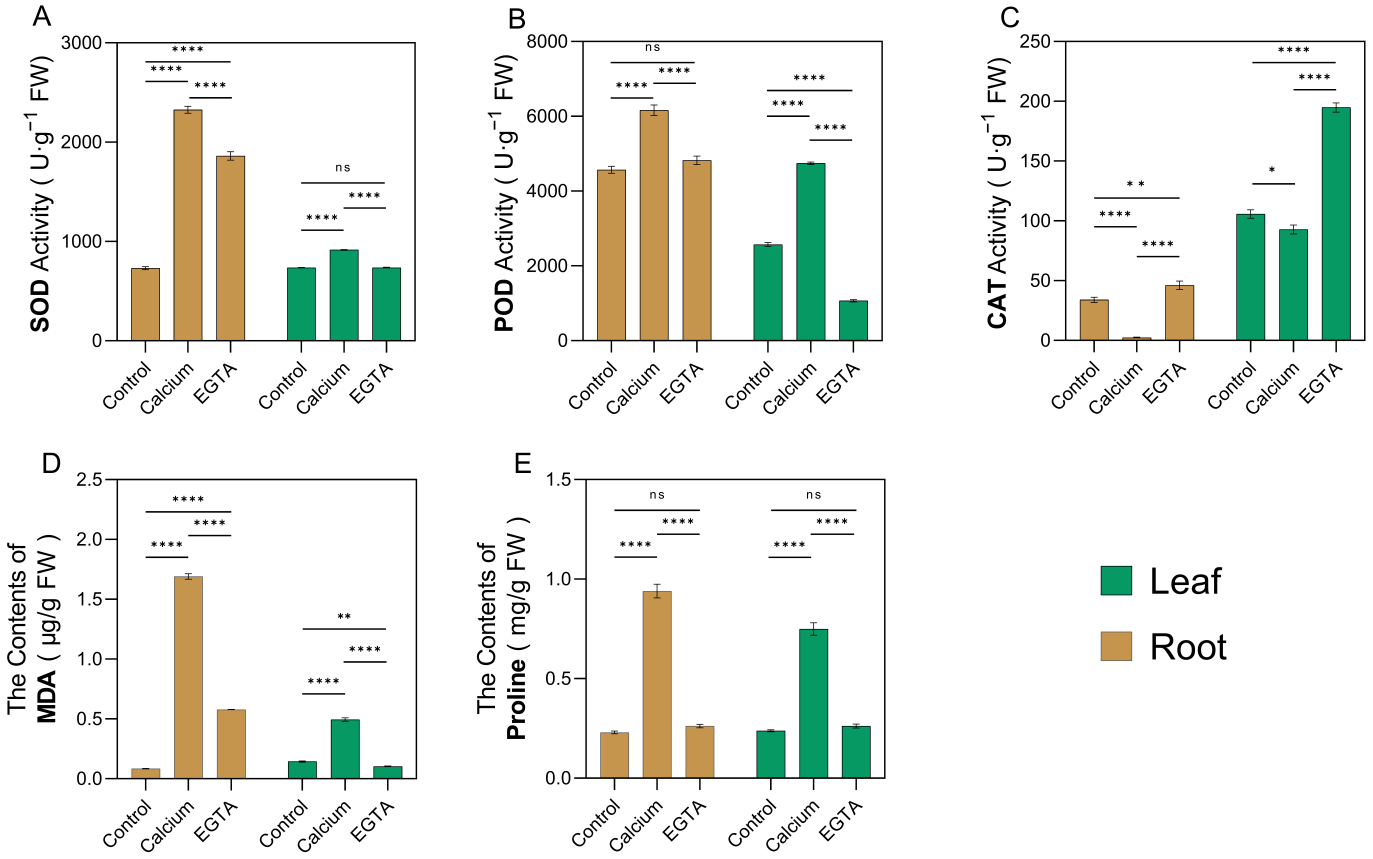


Figure 3. Physiological and biochemical responses of *C. saxicola* roots and leaves to different calcium treatments. (**A**) SOD activity; (**B**) POD activity; (**C**) CAT activity; (**D**) MDA content; (**E**) proline content. Brown and green bars represent roots and leaves, respectively. Data are the mean ± SD ($n = 3$ independent biological replicates from different plants). ns, $p \geq 0.05$; * $p < 0.05$; ** $p < 0.01$; **** $p < 0.0001$. Treatments were Control (deionized water), Calcium (100 mM $CaCl_2$), and EGTA (100 mM $CaCl_2$ plus 100 mM EGTA), applied for six months.

3.4. Root and Leaf Calcium Concentrations and Subcellular Partitioning

ICP-OES measurements showed treatment-dependent changes in root and leaf calcium concentrations (Figure 4A). In the Control group, calcium concentrations were 9.75 ± 0.12 g kg^{-1} dry weight in roots and 17.14 ± 0.10 g kg^{-1} dry weight in leaves. Calcium treatment increased these values to 73.60 ± 0.90 and 54.91 ± 2.10 g kg^{-1} dry weight, respectively, corresponding to 7.55-fold and 3.20-fold the Control concentrations. With EGTA, root and leaf calcium concentrations decreased to 16.25 ± 0.23 and 24.41 ± 1.38 g kg^{-1} dry weight, respectively, but remained above the corresponding Control values. Leaf calcium concentrations exceeded root concentrations in the Control and EGTA groups, whereas root concentrations exceeded leaf concentrations in the Calcium group. Thus, long-term

$CaCl_2$ treatment increased calcium concentrations in both tissues, with a greater relative increase in roots; EGTA attenuated this increase without restoring either tissue to the Control concentration.

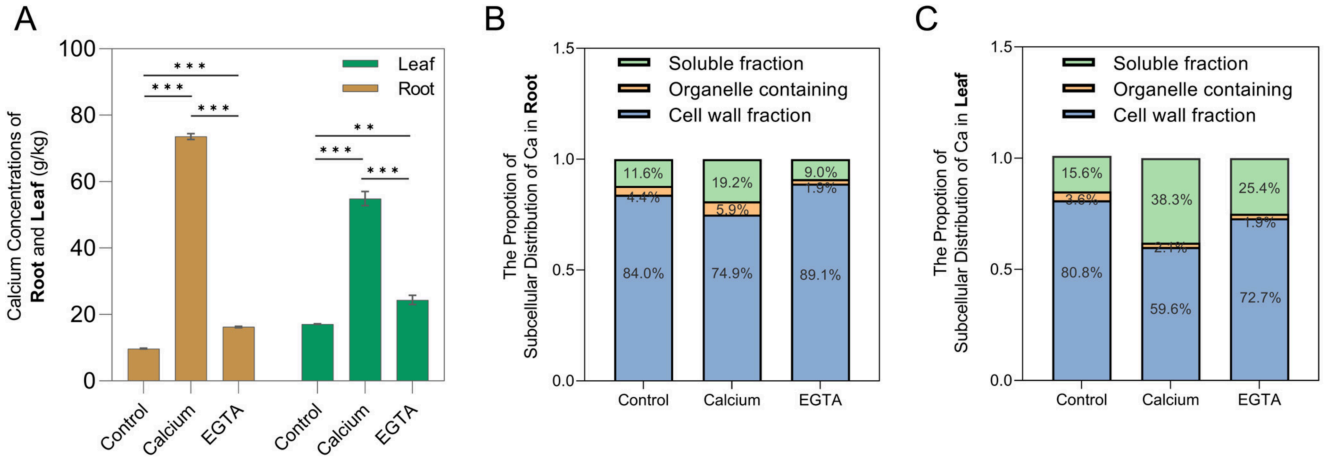


Figure 4. Tissue calcium concentrations and subcellular calcium partitioning in *C. saxicola* under different calcium treatments. (**A**) Calcium concentrations in dried roots and leaves measured by ICP-OES (g kg^{-1} dry weight). Brown and green bars represent roots and leaves, respectively. Data are the mean ± SD ($n = 3$ independent biological replicates). Asterisks indicate differences between the connected treatment pairs within each tissue (** $p < 0.01$; *** $p < 0.001$). (**B**,**C**) Subcellular calcium partitioning in roots (**B**) and leaves (**C**). Calcium was fractionated into cell-wall, organelle-containing, and soluble fractions. Values in B and C are mean percentages of the calcium recovered across these three fractions within each tissue, based on three independent biological replicates. Treatments were Control (deionized water), Calcium (100 mM $CaCl_2$), and EGTA (100 mM $CaCl_2$ plus 100 mM EGTA), applied for six months.

Subcellular fractionation showed that most calcium was associated with the cell-wall fraction in both roots and leaves under all treatments (Figure 4B,C). In roots, the cell-wall fraction accounted for 84.0%, 74.9%, and 89.1% in the Control, Calcium, and EGTA groups, respectively, and the soluble fraction accounted for 11.6%, 19.2%, and 9.0%. In leaves, the corresponding cell-wall proportions were 80.8%, 59.6%, and 72.7%, and the soluble proportions were 15.6%, 38.3%, and 25.4%. Thus, Calcium treatment decreased the cell-wall-bound proportion and increased the soluble proportion in both tissues, with a larger shift in leaves. EGTA increased the cell-wall proportion relative to Calcium treatment.

3.5. Root-Tip Ca^{2+} Flux Under Different Calcium Conditions

Non-invasive micro-test technology (NMT) was used to measure net Ca^{2+} flux at the root surface in the root-tip meristematic region in real time (Figure 5A). Root tips in the Control solution showed weak Ca^{2+} influx, with a mean net flux of −290.71 ± 2.52 pmol cm^{-2} s^{-1}. In the Calcium solution, the net direction reversed to strong efflux, with a mean of 19,791.72 ± 178.62 pmol cm^{-2} s^{-1}. In the EGTA solution, strong Ca^{2+} influx was observed, with a mean net flux of −2043.19 ± 16.64 pmol cm^{-2} s^{-1} (Figure 5B). Differences among the three groups were highly significant ($p < 0.0001$). During the 300 s recording period, the Calcium group maintained a high positive flux with some variation, whereas the Control and EGTA groups maintained negative values, indicating net influx (Figure 5C). These results show that *C. saxicola* root tips changed the direction and magnitude of net Ca^{2+} flux according to Ca^{2+} availability in the test solution.

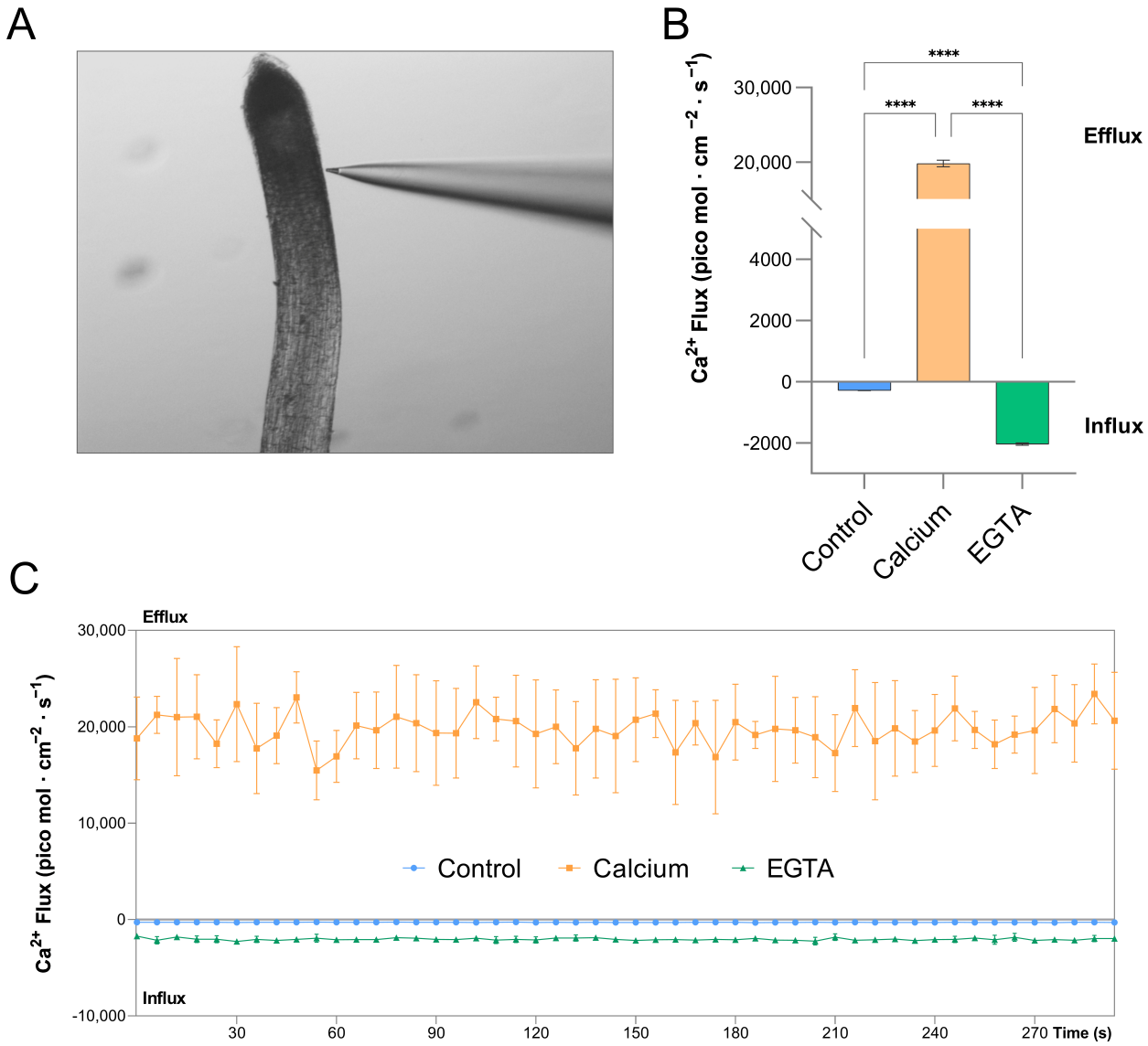


Figure 5. Root-surface net Ca^{2+} flux measured by non-invasive micro-test technology (NMT) in the root-tip meristematic region of *C. saxicola*. (**A**) NMT measurement position. (**B**) Mean net Ca^{2+} flux; positive values indicate net efflux and negative values indicate net influx. Asterisks denote significant differences for the indicated comparisons (**** $p < 0.0001$). (**C**) Net Ca^{2+} flux during the 300 s recording: Calcium samples maintained positive values, whereas Control and EGTA samples maintained negative values. Data are the mean ± SD ($n = 6$ independent plants per treatment). Treatments were Control (deionized water), Calcium (100 mM $CaCl_2$), and EGTA (100 mM $CaCl_2$ plus 100 mM EGTA), applied for six months. Measurements used the corresponding MES-containing test solutions at pH 5.8 described in Section 2.4.

3.6. Total and Major Isoquinoline Alkaloid Contents

Under the chromatographic conditions used, dehydrocavidine, palmatine hydrochloride, and berberine hydrochloride standards produced well-resolved peaks at retention times of 18.126, 23.604, and 27.086 min, respectively (Figure 6A). Calcium treatment significantly increased total alkaloid content in roots and leaves (Figure 6B). Root total alkaloids increased from 6.183 mg g^{-1} in Control to 21.612 mg g^{-1} with Calcium and decreased to 7.841 mg g^{-1} with EGTA. Leaf values increased from 6.370 to 12.942 mg g^{-1} and then decreased to 5.067 mg g^{-1}. The larger increase per unit dry mass indicates a stronger total-alkaloid concentration response in roots. Dehydrocavidine reached 10.054 and 9.443 mg g^{-1} in Calcium-treated roots and leaves, respectively, compared with 4.631 and 2.381 mg g^{-1} in

Control (Figure 6C). EGTA values were 6.923 mg g^{-1} in roots and 1.469 mg g^{-1} in leaves; the leaf value was below Control, whereas the root value remained above or close to Control. Palmatine hydrochloride reached 1.658 and 1.793 mg g^{-1} in Calcium-treated roots and leaves, respectively. In leaves, the EGTA value (0.292 mg g^{-1}) was below the Control value (0.511 mg g^{-1}); in roots, the EGTA value (1.490 mg g^{-1}) did not differ significantly from Calcium (Figure 6D). Berberine hydrochloride reached 1.949 and 1.521 mg g^{-1} in Calcium-treated roots and leaves and decreased in both tissues after EGTA treatment, particularly in leaves (Figure 6E). Overall, long-term high calcium promoted the accumulation of total alkaloids and all three target isoquinoline alkaloids, whereas EGTA generally weakened this effect. Recovery differed among compounds and tissues.

3.7. Transcriptome Assembly and Differential Gene Expression

Eighteen RNA-seq libraries were constructed from roots and leaves of three independent plants in each of the Control, Calcium, and EGTA groups. Paired-end sequencing on an Illumina NovaSeq 6000 generated 123.09 Gb of raw data. After adapter removal and quality filtering, approximately 110.66 Gb of clean data remained, averaging 6.15 Gb per sample (range, 5.27–7.99 Gb). Q30 values ranged from 91.91% to 95.54%, and GC content ranged from 43.27% to 44.13%. De novo assembly of all clean reads with Trinity produced 277,331 transcripts and 72,385 unigenes, with N50 values of 2961 and 2083 bp, respectively. BUSCO analysis detected 1422 complete orthologs among 1614 conserved genes (88.10%), including 1388 complete single-copy and 34 complete duplicated genes; 70 genes were fragmented and 122 were missing. Functional annotation assigned 39,805, 37,582, and 11,316 unigenes to eggNOG, GO, and KEGG, respectively. The assembly therefore covered most conserved genes and provided a suitable basis for expression and functional analyses. Detailed sequencing and quality-control statistics for the 18 RNA-seq libraries are provided in Table S1.

PC1 and PC2 explained 65.49% and 18.41% of expression variance, respectively, accounting for 83.90% in total (Figure 7A). Samples first separated by tissue along PC1, with roots and leaves forming distinct clusters, and then separated by treatment within each tissue along PC2. Biological replicates generally clustered together, indicating good within-group consistency. Differential expression was assessed at $|\log_2 FC| \geq 1$ and FDR < 0.05 using unigenes as the statistical units (Figure 7B). Compared with Control, Calcium treatment produced 6779 root DEGs (3431 upregulated and 3348 downregulated) and 6619 leaf DEGs (2736 upregulated and 3883 downregulated). Relative to Control, EGTA produced 5843 root DEGs (3975 upregulated and 1868 downregulated) but only 881 leaf DEGs (454 upregulated and 427 downregulated). The largest numbers of DEGs occurred in EGTA versus Calcium: 10,542 in roots (6132 upregulated and 4410 downregulated) and 9115 in leaves (6352 upregulated and 2763 downregulated). UpSet analysis showed large shared DEG sets as well as treatment- and tissue-specific sets (Figure 7C). Large root- and leaf-specific intersections under changing calcium availability indicate extensive transcriptional reprogramming with distinct response components in the two tissues.

3.8. KEGG Enrichment and Tissue-Specific Responses

KEGG enrichment of unigenes differentially expressed across the three treatments revealed distinct pathway profiles in roots and leaves (Figure 8). In roots, 10 of the 12 displayed pathways met the significance threshold (BH-adjusted $p < 0.05$): plant hormone signal transduction; phenylalanine, tyrosine, and tryptophan biosynthesis; plant–pathogen interaction; α-linolenic acid metabolism; phenylpropanoid biosynthesis; oxidative phosphorylation; starch and sucrose metabolism; ribosome; isoquinoline alkaloid biosynthesis; and galactose metabolism. Isoquinoline alkaloid biosynthesis included 41 differentially expressed uni-

genes among 57 background unigenes in this pathway (adjusted $p = 0.03147$). Arachidonic acid metabolism and glutathione metabolism were displayed among the highest-ranked pathways but did not meet the threshold (adjusted $p = 0.05455$ and 0.07517, respectively). In leaves, seven displayed pathways were significant: plant hormone signal transduction; photosynthesis–antenna proteins; photosynthesis; circadian rhythm–plant; linoleic acid metabolism; porphyrin and chlorophyll metabolism; and cutin, suberin, and wax biosynthesis. The other five displayed leaf pathways had adjusted $p \geq 0.05$.

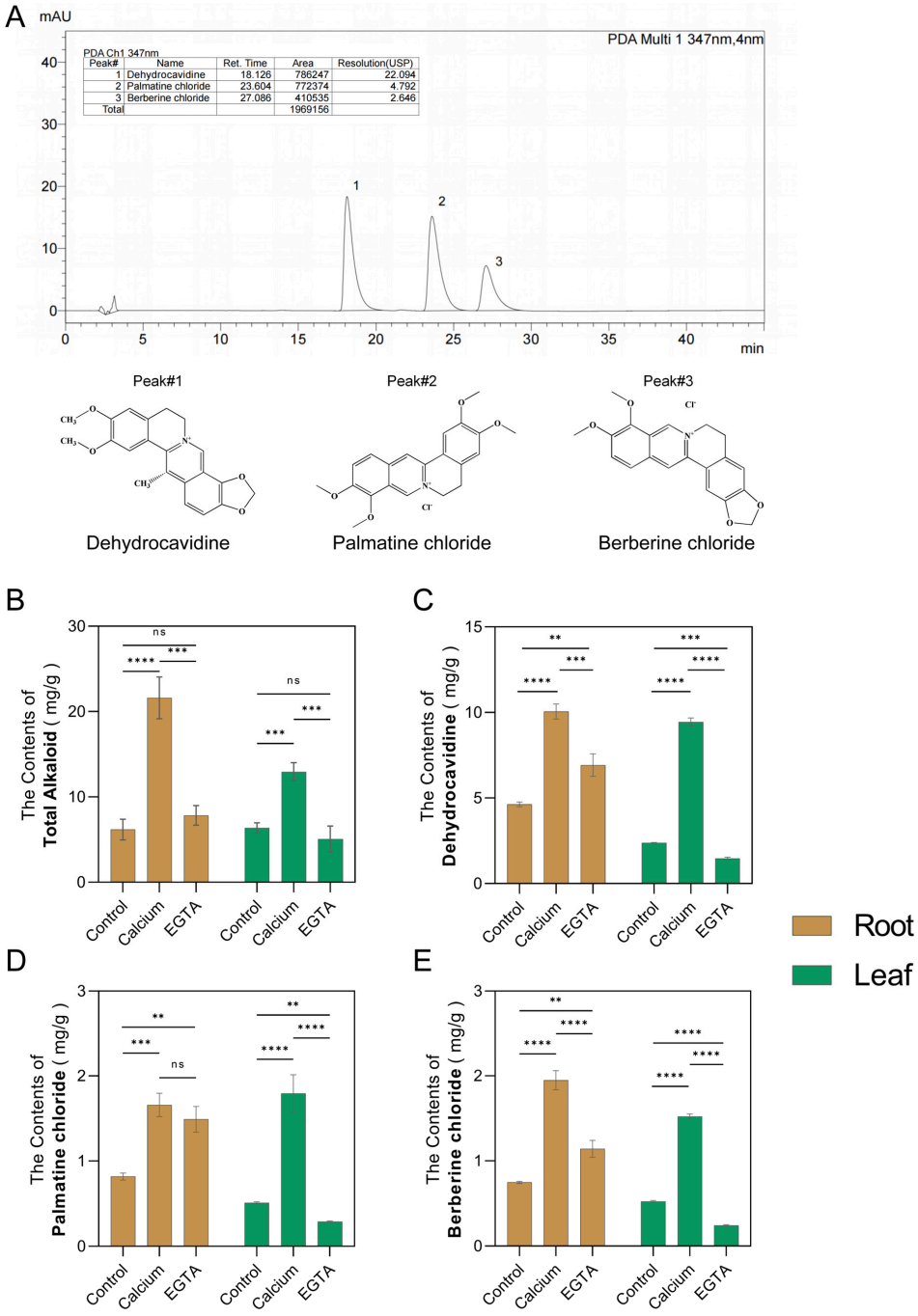


Figure 6. Total alkaloids and three isoquinoline alkaloids in *C. saxicola* roots and leaves under different treatments. (**A**) HPLC chromatograms and chemical structures of dehydrocavidine, palmatine hydrochloride, and berberine hydrochloride standards; (**B**) total alkaloid content; (**C**) dehydrocavidine; (**D**) palmatine hydrochloride; (**E**) berberine hydrochloride. Brown and green bars represent roots and leaves, respectively. Data are the mean ± SD ($n = 3$ independent biological replicates from different

plants). ns, $p \geq 0.05$; ** $p < 0.01$; *** $p < 0.001$; **** $p < 0.0001$. Treatments were Control (deionized water), Calcium (100 mM $CaCl_2$), and EGTA (100 mM $CaCl_2$ plus 100 mM EGTA), applied for six months.

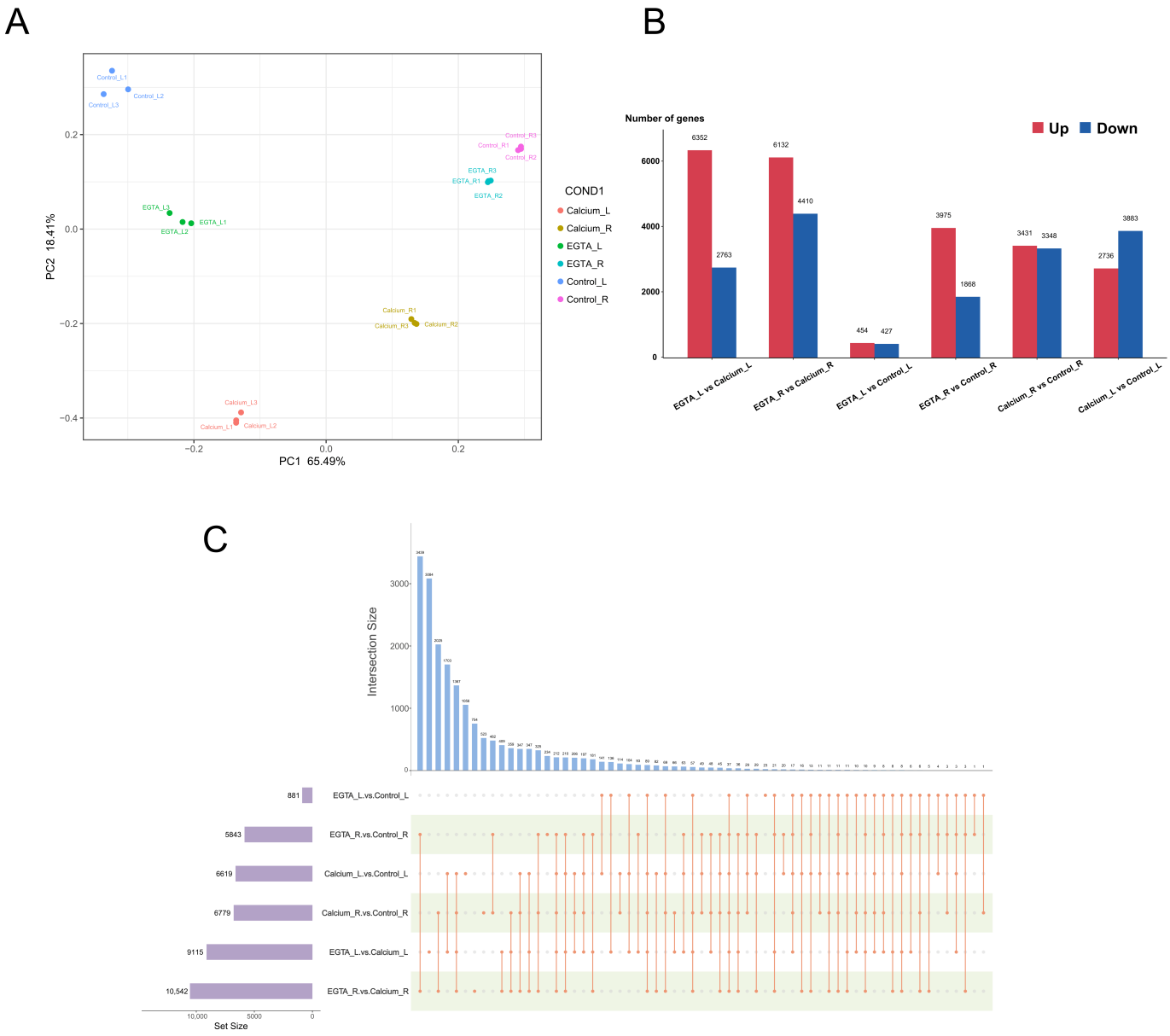


Figure 7. Global transcriptomic features and differentially expressed genes in *C. saxicola* under different calcium treatments. (**A**) Principal component analysis based on gene expression; samples are colored by treatment and tissue (L, leaf; R, root). PC1 and PC2 explain 65.49% and 18.41% of the variance, respectively. (**B**) Numbers of upregulated and downregulated DEGs in pairwise comparisons; red and blue bars indicate upregulated and downregulated genes, respectively. (**C**) UpSet plot showing DEG intersections across six major comparisons. Horizontal bars show the total number of DEGs per comparison, and vertical bars show genes unique to or shared among intersection sets. Pairwise DEGs were defined by $|\log_2 FC| \geq 1$ and BH-FDR < 0.05; directions are relative to the comparison denominator. Each tissue-treatment group contains three independent biological replicates. Treatments were Control (deionized water), Calcium (100 mM $CaCl_2$), and EGTA (100 mM $CaCl_2$ plus 100 mM EGTA), applied for six months.

Plant hormone signal transduction was significantly enriched in both tissues. Significant root pathways included aromatic amino acid and isoquinoline alkaloid biosynthesis, whereas significant leaf pathways included photosynthesis, chlorophyll metabolism, and

epidermal barrier-associated metabolism. Isoquinoline alkaloid biosynthesis was significant in roots but not in leaves. These results identify tissue-specific pathway associations with the three-treatment response; the joint comparison does not assign a common direction of change to an entire pathway.

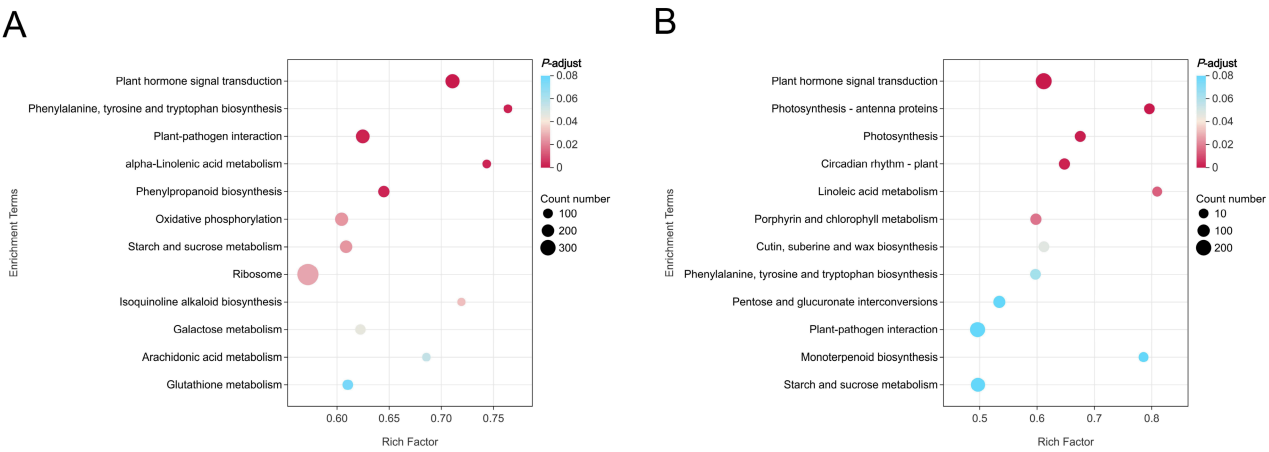


Figure 8. KEGG pathway enrichment of differentially expressed unigenes in *C. saxicola* roots (**A**) and leaves (**B**). Input unigenes were identified by the joint three-treatment test (BH-FDR < 0.05) within each tissue. The 12 pathways with the smallest BH-adjusted enrichment p values are shown; adjusted $p < 0.05$ indicates significant enrichment. Rich factor is the number of differentially expressed unigenes divided by the number of background unigenes in the same pathway. Bubble size indicates the differentially expressed unigene count, and color indicates the adjusted enrichment p value. The background comprised 11,316 KEGG-annotated unigenes. Treatments were Control (deionized water), Calcium (100 mM $CaCl_2$), and EGTA (100 mM $CaCl_2$ plus 100 mM EGTA), applied for six months.

3.9. Expression of Calcium Channels, Ca^{2+}-ATPases, and Calcium-Signaling Genes

Candidate homologous transcripts were identified by sequence-similarity annotation for cyclic nucleotide-gated channels (CNGCs), autoinhibited Ca^{2+}-ATPases (ACAs), calcium-dependent protein kinases (CPKs, also termed CDPKs), calmodulins and calmodulin-like proteins (CaM/CMLs), calcineurin B-like calcium sensors (CBLs), and CBL-interacting protein kinases (CIPKs). Their normalized expression patterns were compared between roots and leaves (Figure 9). The diagram places annotated families in their established functional categories: CNGCs as candidate channels, ACAs as Ca^{2+} pumps, and CPK/CDPK, CaM/CML, and CBL-CIPK as sensing and decoding components. It is a conceptual family-level framework, rather than an experimentally established interaction network in *C. saxicola*. Candidate transcripts differed in their responses to $CaCl_2$ and EGTA and showed clear tissue specificity. Some CNGC- and ACA-related transcripts changed markedly in the Calcium or EGTA groups, whereas CPK-, CaM/CML-, and CBL-CIPK-related transcripts showed diverse treatment and tissue responses. The lack of a uniform direction across roots and leaves suggests that calcium transport, sensing, and decoding modules contribute to tissue-specific responses to calcium availability.

3.10. Transcriptional Responses of Isoquinoline Alkaloid Biosynthetic Genes

To examine the association between calcium availability and isoquinoline alkaloid biosynthesis, transcriptome data were interpreted with reference to the characterized pathway in the congeneric species *Corydalis tomentella* [17]. The pathway heatmap (Figure 10A) summarizes the established conversion of dopamine and 4-hydroxyphenylacetaldehyde (4-HPAA) by norcoclaurine synthase (*NCS*) to (*S*)-norcoclaurine, followed by reactions represented by the annotated *Cs6OMT1*, *CsCNMT*, *CsCYP80B2*, *Cs4′OMT*, and *CsBBE* can-

didates to form downstream products including (*S*)-scoulerine. Most key transcripts were relatively more abundant after Calcium treatment and less abundant after EGTA treatment, especially in roots. This pattern indicates a stronger positive association between calcium availability and transcription of the isoquinoline alkaloid pathway in roots than in leaves.

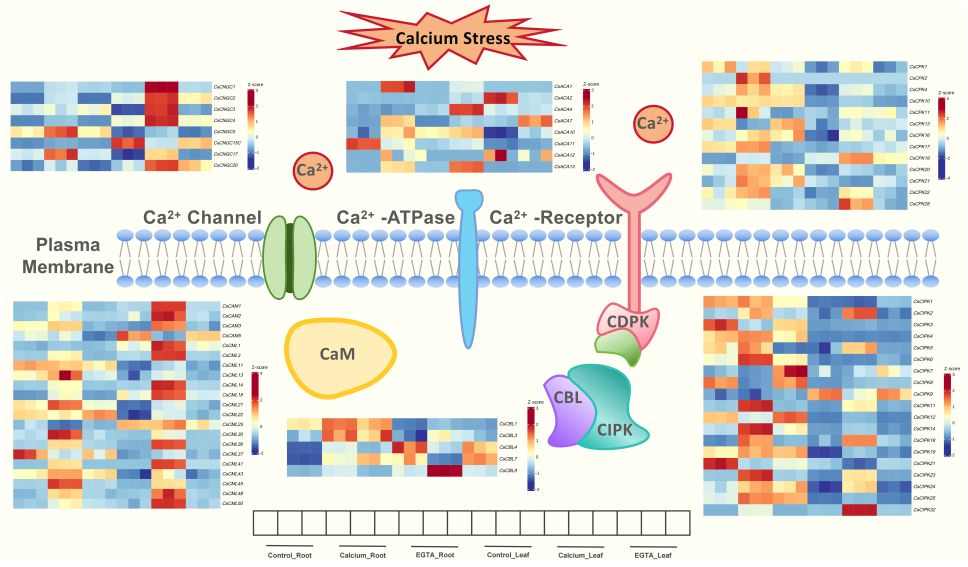


Figure 9. Heatmap of candidate homologous transcripts related to calcium signaling and transport in *C. saxicola* under different calcium treatments. The heatmap shows normalized expression patterns of CNGC-, ACA-, CPK/CDPK-, CaM/CML-, CBL-, and CIPK-related candidate unigenes in Control_Root, Calcium_Root, EGTA_Root, Control_Leaf, Calcium_Leaf, and EGTA_Leaf. Colors indicate *Z*-scores (red, relatively high; blue, relatively low). Row labels are abbreviated candidate transcript names and do not represent formally validated *C. saxicola* gene symbols or confirmed genomic loci. Transcript identifiers and annotations are provided in Table S7. CPK and CDPK denote the same calcium-dependent protein kinase family. Diagram connections summarize known family-level roles and do not demonstrate direct interactions among the displayed candidates. Expression summaries use three independent biological replicates per tissue and treatment. Treatments were Control (deionized water), Calcium (100 mM $CaCl_2$), and EGTA (100 mM $CaCl_2$ plus 100 mM EGTA), applied for six months.

Six candidate transcripts annotated as key biosynthetic enzymes (*CsNCS2*, *Cs6OMT1*, *CsCNMT1*, *CsCYP80B2*, *Cs4′OMT*, and *CsBBE1*) were selected for RT-qPCR validation (Figure 10B–G). In roots, Calcium treatment significantly increased all six transcripts. *CsCNMT1* and *Cs4′OMT* increased by approximately eightfold, whereas *CsBBE1*, *CsNCS2*, *Cs6OMT1*, and *CsCYP80B2* increased by approximately fivefold, fourfold, threefold, and threefold, respectively. After EGTA treatment, root *CsCYP80B2* expression fell below the Control level; *Cs6OMT1* and *CsCNMT1* were close to or below Control; and *Cs4′OMT* and *CsBBE1* were markedly lower than in the Calcium group. *CsNCS2* decreased relative to Calcium but remained above Control. Leaf responses were gene-specific. *CsNCS2* and *Cs4′OMT* tended to decrease after Calcium treatment, whereas *Cs6OMT1*, *CsCNMT1*, *CsCYP80B2*, and *CsBBE1* showed slight increases or small differences among treatments. EGTA more clearly suppressed *Cs4′OMT* and *CsBBE1*, whereas *Cs6OMT1*, *CsCNMT1*, and *CsCYP80B2* showed differing degrees of recovery or maintenance.

Overall, the RT-qPCR patterns were consistent with the transcriptome trends. Calcium-associated induction of isoquinoline alkaloid biosynthetic genes was concentrated in roots, whereas regulation in leaves was more complex and both gene- and tissue-specific.

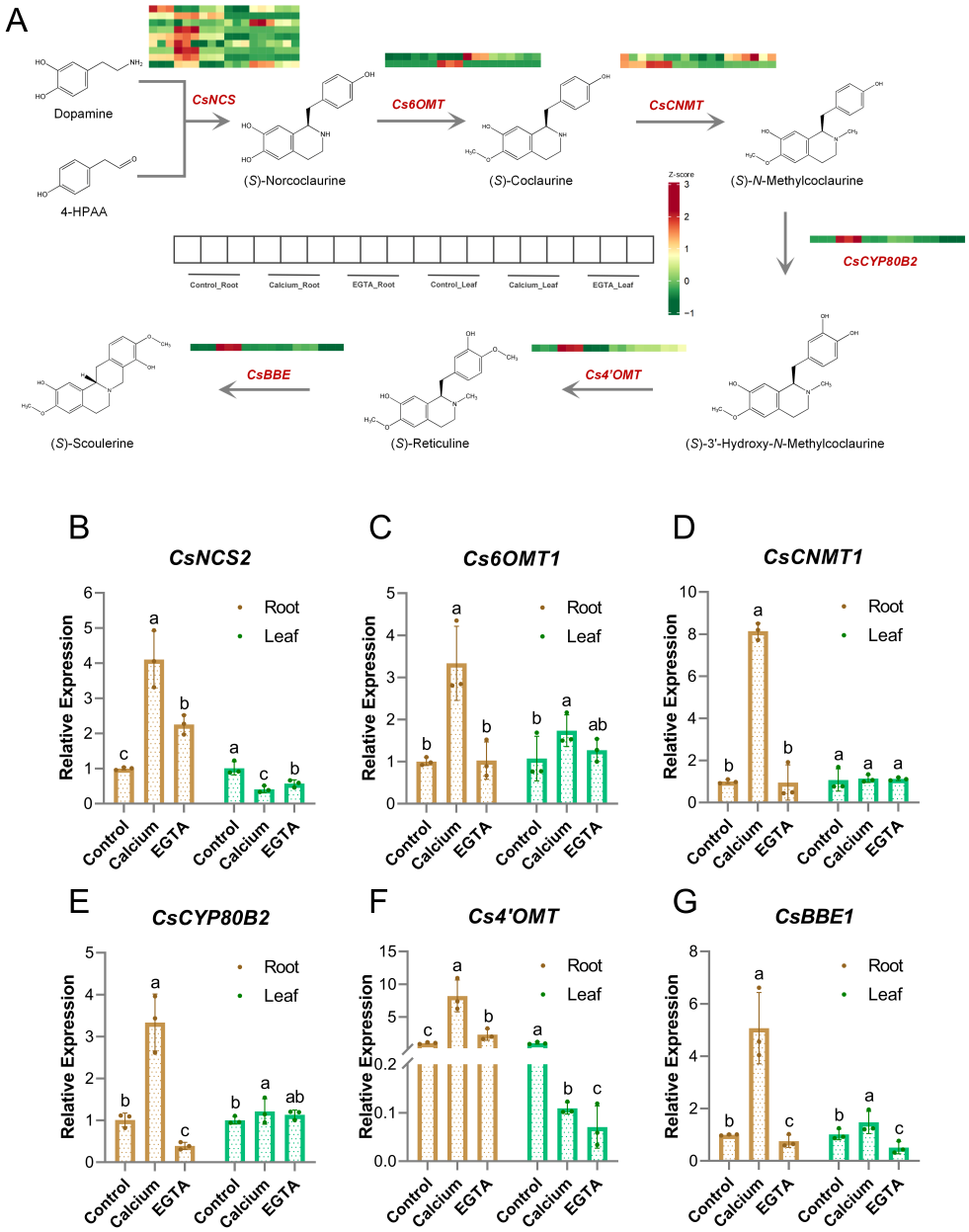


Figure 10. Transcript expression associated with the upstream isoquinoline alkaloid pathway and RT-qPCR validation in *C. saxicola*. (**A**) Literature-based pathway framework and transcriptomic heatmap of annotated candidates in roots and leaves; transcript identifiers and annotations are listed in Table S8. (**B**–**G**) Relative expression of *CsNCS2*, *Cs6OMT1*, *CsCNMT1*, *CsCYP80B2*, *Cs4′OMT*, and *CsBBE1*, respectively, normalized to the reference gene RPL4 (ribosomal protein L4). NCS, norcoclaurine synthase; 6OMT, norcoclaurine 6-O-methyltransferase; CNMT, coclaurine N-methyltransferase; CYP80B2, cytochrome P450 family 80 subfamily B polypeptide 2; 4′OMT, 3′-hydroxy-N-methylcoclaurine 4′-O-methyltransferase; BBE, berberine bridge enzyme; Cs denotes *C. saxicola*. RT-qPCR data are the mean ± SD ($n = 3$ independent biological replicates from different plants). Different lowercase letters indicate significant treatment differences within a tissue (Tukey's test, $p < 0.05$); shared letters indicate no significant difference. Treatments were Control (deionized water), Calcium (100 mM $CaCl_2$), and EGTA (100 mM $CaCl_2$ plus 100 mM EGTA), applied for six months.

3.11. Spatial Distribution of Isoquinoline Alkaloid Pathway Metabolites in Roots

MALDI-MSI was performed on 20 µm main-root transverse sections to compare putatively assigned ions corresponding to L-tyrosine, dopamine, (*S*)-norcoclaurine, (*S*)-3′-hydroxy-N-methylcoclaurine, (*S*)-reticuline, and (*S*)-scoulerine in the Control, Calcium,

and EGTA groups (Figure 11). Average mass spectra are presented in Figure S2, and the six ion assignments are documented in Table S9. Experimental-to-database MS/MS comparisons for L-tyrosine, dopamine, and scoulerine are provided in Figure S3. Because the imaging resolution was 50 µm, periderm, phloem, and xylem regions were assigned by matching ion images to optical images and anatomical landmarks; individual pixels could include multiple cells or adjacent tissues. All treatments showed marked spatial compartmentation. Most assigned metabolite ions were relatively intense in the periderm and weaker near the phloem and xylem, showing higher relative ion signals toward peripheral root tissues. Relative to Control, L-tyrosine and dopamine showed a more pronounced central low-signal region under Calcium, while ions assigned to intermediates from (*S*)-norcoclaurine to (*S*)-scoulerine showed a stronger periphery-to-center gradient. With EGTA, this spatial gradient was less ordered, and some assigned ions showed peripheral high-signal patches and greater internal heterogeneity. The predominant peripheral signal pattern was consistent across the three independent biological samples in each treatment. Thus, the treatments were associated with spatial remodeling of putatively annotated pathway-related ions along the peripheral-to-vascular tissue axis.

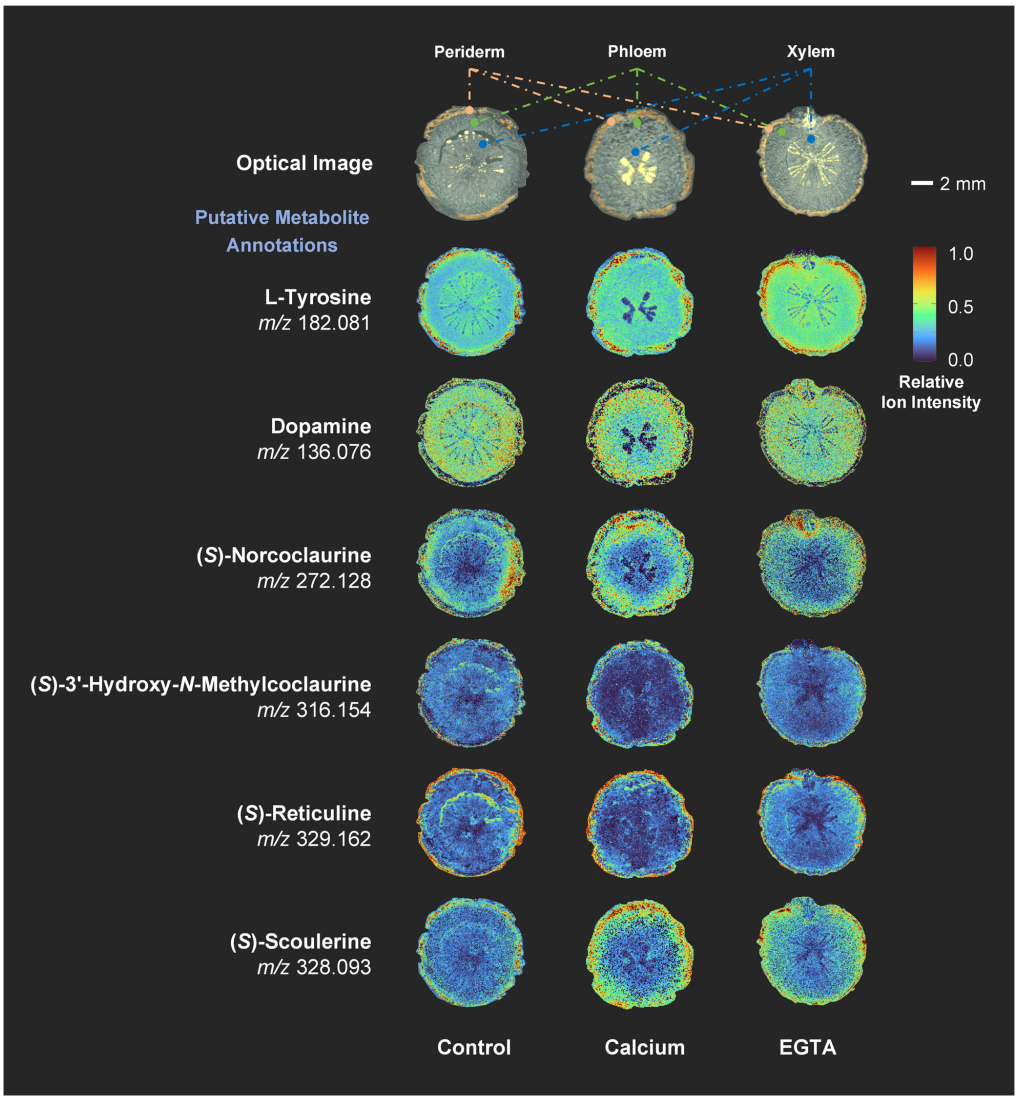


Figure 11. Spatial distribution of putatively assigned benzylisoquinoline alkaloid pathway metabolites in transverse main-root sections of *C. saxicola* under different calcium treatments. MALDI-MSI ion images

were acquired from 20 µm main-root transverse sections from the Control, Calcium, and EGTA groups. Maps are shown for L-tyrosine, dopamine, (*S*)-norcoclaurine, (*S*)-3′-hydroxy-N-methylcoclaurine, (*S*)-reticuline, and (*S*)-scoulerine; corresponding *m*/*z* values are shown in each panel. The color scale represents relative signal intensity (blue, low; red, high). Periderm, phloem, and xylem are labeled from optical and anatomical correspondence. Representative images from three independent plants per treatment are shown; the predominant peripheral signal pattern was consistent across biological replicates. Ion intensities were RMS-normalized and represent relative signals rather than absolute concentrations. Tissue-dependent ion suppression and matrix effects can affect signal intensity; the 50 µm spatial resolution does not resolve individual cells. Putative assignments and their MS1 or MS/MS matching evidence are summarized in Table S9; average mass spectra and selected experimental-to-database MS/MS comparisons are provided in Figures S2 and S3, respectively. Treatments were Control (deionized water), Calcium (100 mM $CaCl_2$), and EGTA (100 mM $CaCl_2$ plus 100 mM EGTA), applied for six months.

4. Discussion

Plants absorb most calcium through their roots, but high external calcium is not necessarily beneficial. Species differ markedly in calcium uptake, tissue homeostasis, and inter-organ transport, and some experience high-calcium stress [1]. Karst soils are commonly rich in exchangeable calcium and carbonates and can contain nearly three times as much calcium as acidic soils [18]. Karst plants may display calcicole, calcifuge, or calcium-indifferent strategies, reflecting different adaptations to heterogeneous soil calcium [19]. Tolerance of high-calcium environments has been associated with foliar calcium partitioning, sequestration, or chelation [20]. In *C. saxicola*, the greater fold increase in root calcium concentration, together with changes in subcellular calcium fractions, indicates tissue-specific responses to prolonged $CaCl_2$ exposure. Because chloride-matched and isoosmotic controls were not included, the responses cannot be attributed specifically to Ca^{2+} independently of Cl^- and osmotic effects. EGTA preferentially chelates Ca^{2+} but can also alter other metal-ion availability in a pH-dependent manner [13]; consequently, its effects are interpreted as responses to the chelation treatment, rather than as a calcium-specific reversal. The measured residual free Ca^{2+} in the EGTA irrigation solution also shows that equimolar $CaCl_2$ and EGTA did not eliminate free calcium. Nevertheless, the observed tissue calcium concentrations and subcellular partitioning patterns provide evidence relevant to adaptation to calcium-rich karst habitats.

4.1. Oxidative Stress and Tissue Remodeling Under Prolonged $CaCl_2$ Exposure

Microscopy and physiological assays together characterized the response to long-term high calcium. SEM and TEM showed that $CaCl_2$ treatment particularly affected interfaces exposed to the external environment: root hairs became disordered, the continuity of thick-walled root tissues decreased, and surface relief increased on stem papillae and stomatal complexes. These changes suggest that cell-wall and epidermal barriers may participate in regulating Ca^{2+} flux and tissue water status; Ca^{2+} cross-linking with cell-wall pectins and the plasticity of root endodermal barriers provide a structural basis for this interpretation [1,21]. SOD and POD activities generally increased in Calcium-treated roots and leaves, together with MDA and proline. These responses corresponded to plasmolysis, cytoplasmic condensation, and increased osmiophilic granules in root cells, consistent with altered tissue calcium status, membrane lipid peroxidation, and osmotic adjustment during $CaCl_2$ exposure. ROS can damage cells but also activate defense gene expression; increased antioxidant activity indicates induced scavenging capacity, whereas the accompanying rise in MDA shows that this capacity did not fully prevent lipid peroxidation [22,23]. Proline may contribute to osmotic balance, protein protection, and redox regulation, but its accumulation alone does not demonstrate increased tolerance [6]. CAT activity differed between tissues:

it decreased markedly in Calcium-treated roots but only slightly in leaves and recovered in both tissues with EGTA. Roots may respond more directly to external Ca^{2+} and ionic strength, whereas leaves may depend more strongly on CAT or other pathways that remove hydrogen peroxide.

4.2. Tissue Calcium Accumulation, Subcellular Partitioning, and Root-Tip Ca^{2+} Flux

Calcium treatment increased root and leaf calcium concentrations to 7.55-fold and 3.20-fold their respective Control values. Although leaves had higher calcium concentrations than roots in the Control and EGTA groups, this relationship was reversed under Calcium treatment. These concentration profiles demonstrate a stronger calcium accumulation response per unit dry mass in roots. EGTA reduced calcium concentrations in both tissues relative to Calcium treatment, but values remained above Control, indicating partial attenuation of tissue calcium accumulation. Plant Ca^{2+} homeostasis depends on the coordinated actions of nonselective cation channels, intracellular storage, membrane transport, and root-shoot transport rather than on a single transport step [24,25]. Together with the changes in root-tip net Ca^{2+} flux and subcellular fractions, the concentration data support tissue-specific adjustments in calcium handling. They do not quantify whole-plant calcium allocation or establish a change in root-to-leaf transport.

At the subcellular level, most calcium was recovered in the operationally defined cell-wall fraction in both tissues. Calcium treatment decreased this fraction from 84.0% to 74.9% in roots and from 80.8% to 59.6% in leaves, while increasing the soluble fraction from 11.6% to 19.2% in roots and from 15.6% to 38.3% in leaves. These changes demonstrate redistribution among the cell-wall, organelle-containing, and soluble fractions, particularly toward soluble calcium. The soluble fraction may include vacuolar and other intracellular calcium, but the present fractionation cannot establish vacuolar localization. It should therefore be distinguished from molecular evidence involving transporters such as CAX. The CBL-CIPK module can regulate tonoplast CAX systems and cytosolic calcium homeostasis [3]. The fractionation results are consistent with a change in intracellular buffering but do not identify a specific compartment or transporter.

The periderm and endodermis form important root–environment interfaces and radial transport barriers. Lignified and suberized barriers limit nonselective radial diffusion and contribute to environmental protection [26,27]. NMT measurements showed weak net Ca^{2+} influx in the Control solution, strong net efflux in the Calcium solution, and stronger net influx in the EGTA solution. These differences reflect treatment-associated calcium exchange at the root surface under the respective assay conditions and are relevant to local ion exchange at the root–solution interface. Because net flux is the balance between inward and outward movement, the positive Calcium values indicate that outward movement exceeded inward movement during measurement; they do not quantify cumulative calcium uptake over six months. Such regulation of local ion exchange is consistent with established roles of cation channels and calcium-signaling systems in plant ion homeostasis [24].

4.3. Alkaloid Accumulation and Biosynthetic Gene Expression Respond Primarily in Roots

Roots are directly exposed to soil particles, rhizosphere microorganisms, and potential pathogens, and are protected by both structural barriers, including the periderm and endodermis, and specialized metabolites [27,28]. Protoberberine alkaloids can accumulate in a cell type-specific manner near peridermal barriers, forming a potential chemical defense layer [29]. Root exudates also reshape rhizosphere microbial communities through specialized metabolic networks, with consequences for plant growth and defense [30–32]. Tissue-level accumulation in roots may therefore reflect chemical protection or microbial interactions at the root-soil interface rather than only whole-plant metabolic activity. The

ecological roles of specialized metabolites depend on their tissue location, environmental context, and broader metabolic state [33].

Total alkaloid assays and HPLC showed that Calcium treatment increased total alkaloids and the three target compounds in roots and leaves, with a larger increase in root total alkaloids. EGTA generally reduced this accumulation, although the degree of recovery varied by compound and tissue. Roots exposed to soil organisms and belowground herbivores can develop tissue- and metabolite-specific defense systems [34]. The stronger root response observed here may reflect increased investment in defensive or specialized metabolism at the belowground interface. However, changes in metabolite content cannot establish a direct effect of calcium on a specific enzymatic step and could also reflect growth dilution, transport, storage, or turnover.

Transcriptome and RT-qPCR data provided corresponding expression evidence. Root *CsNCS2*, *Cs6OMT1*, *CsCNMT1*, *CsCYP80B2*, *Cs4′OMT*, and *CsBBE1* were induced by Calcium treatment, particularly *CsCNMT1* and *Cs4′OMT*, and most decreased with EGTA. These enzymes occur in consecutive steps or branch points in benzylisoquinoline alkaloid biosynthesis, and cytochrome P450s and methyltransferases can influence structural diversity and metabolic flux [35–39]. The agreement between root transcript abundance and target alkaloid content supports a coordinated transcriptional response under high calcium. The six genes responded less uniformly in leaves: some increased slightly, whereas others were unchanged or decreased, and EGTA effects were gene-specific. This root-leaf difference is consistent with the HPLC data and identifies roots as the tissue with the stronger association between treatment, biosynthetic transcript abundance, and alkaloid concentration, whereas leaves may contribute more to photosynthesis and carbon supply. Gene expression and metabolite accumulation need not change in parallel, because enzyme activity, substrate supply, transport, storage, and turnover also regulate metabolite abundance [40].

4.4. Spatial Metabolism and Tissue-Specific Transcription Support a Multiscale Response

PCA separated roots and leaves along PC1, showing that tissue identity was the main source of transcriptomic variation, while treatments separated within each tissue along PC2. Significant root enrichment involved hormone signaling, aromatic amino acid biosynthesis, and isoquinoline alkaloid biosynthesis; significant leaf pathways included photosynthesis, porphyrin and chlorophyll metabolism, and cutin, suberin, and wax biosynthesis. Glutathione metabolism ranked among the displayed root pathways but did not meet the BH-adjusted significance threshold. This division corresponds to the physiological and metabolic phenotypes: roots showed stronger ion and specialized-metabolic regulation, whereas leaves emphasized maintenance of photosynthetic and epidermal systems. Calcium signaling itself depends on channels, Ca^{2+} pumps, antiporters, and sensing and decoding modules [23,25]. The diverse expression of individual CNGC, ACA, CPK, CaM/CML, CBL, and CIPK candidates identifies multiple family members as candidates for tissue-specific transport and signal decoding; the expression data do not establish direct regulatory interactions.

MALDI-MSI provides anatomical context for interpreting metabolite synthesis, transport, and storage by preserving spatial information [41–43]. Here, bulk HPLC measurements were complemented by spatial ion signals putatively assigned to L-tyrosine, dopamine, and several isoquinoline alkaloid intermediates in the periderm, phloem, and xylem regions of root transverse sections. Signals were spatially compartmented and generally stronger near the periderm. Calcium and EGTA treatments produced different peripheral-to-central gradients and local heterogeneity, corresponding to changes in alkaloid content and root biosynthetic gene expression. Casparian bands have been documented in the periderm of Pelargonium hortorum [44], providing comparative context

for considering the peripheral root region as a structural and metabolic interface. In *C. saxicola*, the peripheral signal distribution suggests a possible interface-associated role for these metabolites. This distribution is consistent with the barrier and selective transport functions of the periderm and endodermis at the root-soil interface [26]. Matrix effects and tissue-dependent ion suppression can alter relative signal intensity, so weak signal does not necessarily indicate proportionally low absolute content. Moreover, 50 μm pixels can include multiple cells or adjacent tissues, limiting attribution to individual cell types. Nevertheless, the spatial data extend bulk alkaloid measurements to specific anatomical interfaces. The coordinated changes in root alkaloid content, associated transcripts, and spatial patterns support the working hypothesis that isoquinoline alkaloids contribute to root-soil interface protection under high calcium. This remains a protective hypothesis supported by spatial and expression associations, rather than a demonstrated defense mechanism.

5. Conclusions

Integrated physiological, transcriptomic, chemical, and spatial mass spectrometry analyses showed that prolonged $CaCl_2$ exposure was accompanied by increased lipid peroxidation in *C. saxicola* roots and leaves and structural changes in roots, stems, and leaves. Calcium concentrations increased in roots and leaves, with a greater fold increase in roots, accompanied by altered root-tip net Ca^{2+} flux and redistribution between cell-wall and soluble fractions. EGTA attenuated the concentration increases, although both tissues remained above their Control levels. These findings indicate tissue-specific calcium accumulation and subcellular adjustments during prolonged $CaCl_2$ exposure. Altered calcium availability was also associated with the expression of isoquinoline alkaloid biosynthetic genes, accumulation of target alkaloids, and changes in their spatial patterns in roots. Leaf responses more strongly involved photosynthesis, chlorophyll metabolism, and epidermal barrier processes. Together, these findings define tissue-specific physiological and metabolic responses in the $CaCl_2$/EGTA treatment context and identify candidate genes for subsequent functional characterization. The association of peripheral root signals with alkaloid accumulation and transcript changes supports a testable root-interface protection hypothesis, without establishing direct calcium regulation of alkaloid biosynthesis.

Supplementary Materials: The following supporting information can be downloaded at: https://www.mdpi.com/article/10.3390/horticulturae12111439/s1, Table S1: Global overview of transcriptome sequencing data; Table S2: RPL4 transcript annotation; Table S3: RPL4 expression in the transcriptome; Table S4: RPL4 pairwise differential expression statistics; Table S5: RT-qPCR reaction mixture; Table S6: Reference and target gene primers used in RT-qPCR; Table S7: Candidate transcript identifiers and annotations shown in Figure 9; Table S8: Candidate transcript identifiers and annotations shown in Figure 10; Table S9: Putative annotations and mass spectral matching information for six metabolite-related ions detected by MALDI-MSI in *C. saxicola* roots; Figure S1: Free Ca^{2+} concentrations in irrigation solutions and final total calcium content in pot substrate; Figure S2: Average MALDI-MSI mass spectra of root sections under the three treatments; Figure S3: Experimental and database MS/MS spectra supporting putative metabolite annotations in roots.

Author Contributions: Conceptualization, Q.G. and H.S.; methodology, Q.G. and K.Z.; software, Y.D.; validation, C.L. and Y.D.; formal analysis, T.W.; investigation, T.W., Q.Z. and C.L.; resources, Q.G. and K.Z.; data curation, C.L.; writing—original draft preparation, C.L.; writing—review and editing, Q.G.; supervision, H.S.; project administration, Q.G.; funding acquisition, Q.G. All authors have read and agreed to the published version of the manuscript.

Funding: This research was funded by the Jiangsu Modern Agricultural Industry Technology System Construction Project, grant number JATS [2023] 419, Jiangsu Provincial Department of Agriculture and Rural Affairs, Nanjing 210000, China.

Institutional Review Board Statement: Not applicable.

Data Availability Statement: The raw sequence data reported in this paper have been deposited in the Genome Sequence Archive in National Genomics Data Center, China National Center for Bioinformation/Beijing Institute of Genomics, Chinese Academy of Sciences (GSA: CRA051136), and are publicly accessible at https://ngdc.cncb.ac.cn/gsa (accessed on 1 October 2026). Further inquiries may be directed to the corresponding author.

Acknowledgments: We thank Zhongfu Wei for assistance in the resource survey and assessment of *C. saxicola* in Donglan County, and Nanjing Zhongshan Pharmaceutical Co., Ltd. for assistance with the HPLC analyses. The AI tools used in this study were DeepSeek (DeepSeek-V4.1-Flash; Hangzhou DeepSeek Artificial Intelligence Basic Technology Research Co., Ltd., Hangzhou, China) and ChatGPT (GPT-5.6-Sol, 2026 release; OpenAI, San Francisco, CA, USA). The authors have reviewed and edited the output and take full responsibility for the content of this publication.

Conflicts of Interest: Author Kaijun Zhao was employed by the company Nanjing Zhongshan Pharmaceutical Co., Ltd., Nanjing, China. The remaining authors declare that the research was conducted in the absence of any commercial or financial relationships that could be construed as potential conflicts of interest.

References

1. White, P.J.; Broadley, M.R. Calcium in plants. *Ann. Bot.* **2003**, *92*, 487–511. [CrossRef] [PubMed]
2. Feng, D.; Wang, X.J.; Gao, J.P.; Zhang, C.X.; Liu, H.; Liu, P.; Sun, X.A. Exogenous calcium: Its mechanisms and research advances involved in plant stress tolerance. *Front. Plant Sci.* **2023**, *14*, 1143963. [CrossRef] [PubMed]
3. Wang, C.; Tang, R.-J.; Kou, S.; Xu, X.; Lu, Y.; Rauscher, K.; Voelker, A.; Luan, S. Mechanisms of calcium homeostasis orchestrate plant growth and immunity. *Nature* **2024**, *627*, 382–388. [CrossRef] [PubMed]
4. Mittler, R.; Zandalinas, S.I.; Fichman, Y.; Van Breusegem, F. Reactive oxygen species signalling in plant stress responses. *Nat. Rev. Mol. Cell Biol.* **2022**, *23*, 663–679. [CrossRef] [PubMed]
5. Dumanović, J.; Nepovimova, E.; Natić, M.; Kuča, K.; Jaćević, V. The significance of reactive oxygen species and antioxidant defense system in plants: A concise overview. *Front. Plant Sci.* **2021**, *11*, 552969. [CrossRef] [PubMed]
6. Ghosh, U.K.; Islam, M.N.; Siddiqui, M.N.; Cao, X.; Khan, M.A.R. Proline, a multifaceted signalling molecule in plant responses to abiotic stress: Understanding the physiological mechanisms. *Plant Biol.* **2022**, *24*, 227–239. [CrossRef] [PubMed]
7. Qin, F.; Chen, Y.; Wang, F.F.; Tang, S.Q.; Fang, Y.L. *Corydalis saxicola* Bunting: A review of its traditional uses, phytochemistry, pharmacology, and clinical applications. *Int. J. Mol. Sci.* **2023**, *24*, 1626. [CrossRef] [PubMed]
8. Xie, G.Y.; Jin, S.Y.; Li, H.T.; Ai, M.K.; Han, F.; Dai, Y.Q.; Tao, W.; Zhu, Y.; Zhao, Y.C.; Qin, M.J. Chemical constituents and antioxidative, anti-inflammatory and anti-proliferative activities of wild and cultivated *Corydalis saxicola*. *Ind. Crops Prod.* **2021**, *169*, 113647. [CrossRef]
9. Li, C.; Liu, H.; Qin, M.; Tan, Y.-J.; Ou, X.-L.; Chen, X.-Y.; Wei, Y.; Zhang, Z.-J.; Lei, M. RNA editing events and expression profiles of mitochondrial protein-coding genes in the endemic and endangered medicinal plant, *Corydalis saxicola*. *Front. Plant Sci.* **2024**, *15*, 1332460. Correction in *Front. Plant Sci.* **2026**, *17*, 1783725. https://doi.org/10.3389/fpls.2026.1783725. [CrossRef] [PubMed]
10. Cheng, X.X.; Wang, D.M.; Jiang, L.; Yang, D.P. Simultaneous determination of eight bioactive alkaloids in *Corydalis saxicola* by high-performance liquid chromatography coupled with diode array detection. *Phytochem. Anal.* **2008**, *19*, 420–428. [CrossRef] [PubMed]
11. Wang, Q.-Z.; Liang, J.-Y.; Yuan, Y. Chemical constituents of *Corydalis saxicola*. *Chin. J. Nat. Med.* **2007**, *5*, 31–34.
12. Qin, F.; Dai, L.M.; Zhang, B.; Huang, R.Z.; Wang, F.F.; Qin, J.K.; Liang, D.; Wang, H.S. (±)-Corysaxicolaine A: A pair of antitumor enantiomeric alkaloid dimers from *Corydalis saxicola*. *Org. Biomol. Chem.* **2022**, *20*, 1396–1400. [CrossRef] [PubMed]
13. De Vriese, K.; Costa, A.; Beeckman, T.; Vanneste, S. Pharmacological strategies for manipulating plant Ca^{2+} signalling. *Int. J. Mol. Sci.* **2018**, *19*, 1506. [CrossRef] [PubMed]
14. Liu, Y.J.; Yu, X.F.; Feng, Y.M.; Zhang, C.; Wang, C.; Zeng, J.; Huang, Z.; Kang, H.Y.; Fan, X.; Sha, L.N.; et al. Physiological and transcriptome response to cadmium in cosmos (*Cosmos bipinnatus* Cav.) seedlings. *Sci. Rep.* **2017**, *7*, 14691. [CrossRef] [PubMed]
15. Sun, Q.; Chen, H.; Lin, Q.; Wu, Y.; Lei, Y.; Luo, X.; Li, N.; Xu, L.; Zhou, S.; Cheng, J.; et al. Integrated pharmacokinetic properties and tissue distribution of *Corydalis saxicola* Bunting total alkaloids in HFHCD-induced mice: Implications for pharmacokinetic variability in MASH treatment. *Biomed. Pharmacother.* **2025**, *192*, 118665. [CrossRef] [PubMed]
16. Deininger, S.O.; Cornett, D.S.; Paape, R.; Becker, M.; Pineau, C.; Rauser, S.; Walch, A.; Wolski, E. Normalization in MALDI-TOF imaging datasets of proteins: Practical considerations. *Anal. Bioanal. Chem.* **2011**, *401*, 167–181. [CrossRef] [PubMed]
17. Xu, Z.; Li, Z.; Ren, F.; Gao, R.; Wang, Z.; Zhang, J.; Zhao, T.; Ma, X.; Pu, X.; Xin, T.; et al. The genome of *Corydalis* reveals the evolution of benzylisoquinoline alkaloid biosynthesis in Ranunculales. *Plant J.* **2022**, *111*, 217–230. [CrossRef] [PubMed]

18. Huang, Q.H.; Cai, Y.L. Spatial pattern of karst rock desertification in the middle of Guizhou Province, southwestern China. *Environ. Geol.* **2007**, *52*, 1325–1330. [CrossRef]
19. Ji, F.T.; Li, N.; Deng, X. Calcium content characteristics and high-calcium adaptation patterns of plants in karst areas. *Chin. J. Plant Ecol.* **2009**, *33*, 926–935. (In Chinese)
20. Borer, C.H.; Hamby, M.N.; Hutchinson, L.H. Plant tolerance of a high calcium environment via foliar partitioning and sequestration. *J. Arid Environ.* **2012**, *85*, 128–131. [CrossRef]
21. Hückelhoven, R. Cell wall-associated mechanisms of disease resistance and susceptibility. *Annu. Rev. Phytopathol.* **2007**, *45*, 101–127. [CrossRef] [PubMed]
22. Choudhury, F.K.; Rivero, R.M.; Blumwald, E.; Mittler, R. Reactive oxygen species, abiotic stress and stress combination. *Plant J.* **2017**, *90*, 856–867. [CrossRef] [PubMed]
23. Gilroy, S.; Białasek, M.; Suzuki, N.; Górecka, M.; Devireddy, A.R.; Karpiński, S.; Mittler, R. ROS, calcium, and electric signals: Key mediators of rapid systemic signaling in plants. *Plant Physiol.* **2016**, *171*, 1606–1615. [CrossRef] [PubMed]
24. Demidchik, V.; Maathuis, F.J.M. Physiological roles of nonselective cation channels in plants: From salt stress to signalling and development. *New Phytol.* **2007**, *175*, 387–404. [CrossRef] [PubMed]
25. Kudla, J.; Batistič, O.; Hashimoto, K. Calcium signals: The lead currency of plant information processing. *Plant Cell* **2010**, *22*, 541–563. [CrossRef] [PubMed]
26. Geldner, N. The endodermis. *Annu. Rev. Plant Biol.* **2013**, *64*, 531–558. [CrossRef] [PubMed]
27. Naseer, S.; Lee, Y.; Lapierre, C.; Franke, R.; Nawrath, C.; Geldner, N. Casparian strip diffusion barrier in *Arabidopsis* is made of a lignin polymer without suberin. *Proc. Natl. Acad. Sci. USA* **2012**, *109*, 10101–10106. [CrossRef] [PubMed]
28. Stringlis, I.A.; Yu, K.; Feussner, K.; de Jonge, R.; van Bentum, S.; Van Verk, M.C.; Berendsen, R.L.; Bakker, P.A.H.M.; Feussner, I.; Pieterse, C.M.J. MYB72-dependent coumarin exudation shapes root microbiome assembly to promote plant health. *Proc. Natl. Acad. Sci. USA* **2018**, *115*, E5213–E5222. [CrossRef] [PubMed]
29. Samanani, N.; Yeung, E.C.; Facchini, P.J. Cell type-specific protoberberine alkaloid accumulation in *Thalictrum flavum*. *J. Plant Physiol.* **2002**, *159*, 1189–1196. [CrossRef]
30. Hu, L.; Robert, C.A.M.; Cadot, S.; Zhang, X.; Ye, M.; Li, B.; Manzo, D.; Chervet, N.; Steinger, T.; van der Heijden, M.G.A.; et al. Root exudate metabolites drive plant-soil feedbacks on growth and defense by shaping the rhizosphere microbiota. *Nat. Commun.* **2018**, *9*, 2738. [CrossRef] [PubMed]
31. Huang, A.C.C.; Jiang, T.; Liu, Y.X.; Bai, Y.C.; Reed, J.; Qu, B.Y.; Goossens, A.; Nützmann, H.W.; Bai, Y.; Osbourn, A. A specialized metabolic network selectively modulates *Arabidopsis* root microbiota. *Science* **2019**, *364*, 546–549. [CrossRef] [PubMed]
32. Diab, E.; Du, C.; Tigani, W.; Elsayed, S.S.; van Wezel, G.P. Plant coumarins modulate natural product biosynthesis in a *Streptomyces* root endophyte. *J. Nat. Prod.* **2026**, *89*, 980–991. [CrossRef] [PubMed]
33. Mithöfer, A.; Boland, W. Plant defense against herbivores: Chemical aspects. *Annu. Rev. Plant Biol.* **2012**, *63*, 431–450. [CrossRef] [PubMed]
34. Rasmann, S.; Agrawal, A.A. In defense of roots: A research agenda for studying plant resistance to belowground herbivory. *Plant Physiol.* **2008**, *146*, 875–880. [CrossRef] [PubMed]
35. Williams, D.; De Luca, V. Plant cytochrome P450s directing monoterpene indole alkaloid and benzylisoquinoline alkaloid biosynthesis. *Phytochem. Rev.* **2023**, *22*, 309–338. Correction in *Phytochem. Rev.* **2024**, *23*, 579–581. https://doi.org/10.1007/s11101-023-09885-w. [CrossRef]
36. Facchini, P.J.; De Luca, V. Opium poppy and Madagascar periwinkle: Model non-model systems to investigate alkaloid biosynthesis in plants. *Plant J.* **2008**, *54*, 763–784. [CrossRef] [PubMed]
37. Hong, U.V.T.; Tamiru-Oli, M.; Hurgobin, B.; Lewsey, M.G. Genomic and cell-specific regulation of benzylisoquinoline alkaloid biosynthesis in opium poppy. *J. Exp. Bot.* **2025**, *76*, 35–51. [CrossRef] [PubMed]
38. Hagel, J.M.; Facchini, P.J. Dioxygenases catalyze the O-demethylation steps of morphine biosynthesis in opium poppy. *Nat. Chem. Biol.* **2010**, *6*, 273–275. [CrossRef] [PubMed]
39. Horn, P.J.; Chapman, K.D. Imaging plant metabolism in situ. *J. Exp. Bot.* **2024**, *75*, 1654–1670. [CrossRef] [PubMed]
40. De Luca, V.; St Pierre, B. The cell and developmental biology of alkaloid biosynthesis. *Trends Plant Sci.* **2000**, *5*, 168–173. [CrossRef] [PubMed]
41. Buchberger, A.R.; DeLaney, K.; Johnson, J.; Li, L. Mass spectrometry imaging: A review of emerging advancements and future insights. *Anal. Chem.* **2018**, *90*, 240–265. [CrossRef] [PubMed]
42. Lee, Y.J.; Perdian, D.C.; Song, Z.; Yeung, E.S.; Nikolau, B.J. Use of mass spectrometry for imaging metabolites in plants. *Plant J.* **2012**, *70*, 81–95. [CrossRef] [PubMed]

43. Xu, B.; Chen, L.; Lv, F.; Pan, Y.; Fu, X.; Pei, Z. Visualization of metabolites identified in the spatial metabolome of traditional Chinese medicine using DESI-MSI. *J. Vis. Exp.* **2022**, *190*, e64912. [CrossRef] [PubMed]
44. Meyer, C.J.; Peterson, C.A. Casparian bands occur in the periderm of *Pelargonium hortorum* stem and root. *Ann. Bot.* **2011**, *107*, 591–598. [CrossRef] [PubMed]

Disclaimer/Publisher's Note: The statements, opinions and data contained in all publications are solely those of the individual author(s) and contributor(s) and not of MDPI and/or the editor(s). MDPI and/or the editor(s) disclaim responsibility for any injury to people or property resulting from any ideas, methods, instructions or products referred to in the content.